Cellular/Molecular

SMARCA4 Loss and Mutated β-Catenin Induce Proliferative Lesions in the Murine Embryonic Cerebellum

Carolin Göbel,[1,2] Melanie Schoof,[1,2] Dörthe Holdhof,[1,2] Michael Spohn,[2,3] and Ulrich Schüller[1,2,4]

[1]Department of Pediatric Hematology and Oncology, University Medical Center Hamburg-Eppendorf, Hamburg D-20251, Germany, [2]Research Institute Children's Cancer Center Hamburg, Hamburg D-20251, Germany, [3]Bioinformatics Core, University Medical Center Hamburg-Eppendorf, Hamburg D-20251, Germany, and [4]Institute of Neuropathology, University Medical Center Hamburg-Eppendorf, Hamburg D-20251, Germany

Almost all medulloblastomas (MB) of the Wingless/Int-1 (WNT) type are characterized by hotspot mutations in *CTNNB1*, and mouse models have convincingly demonstrated the tumor-initiating role of these mutations. Additional alterations in *SMARCA4* are detected in ∼20% of WNT MB, but their functional role is mostly unknown. We, therefore, amended previously described brain lipid binding protein (*Blbp*)-*cre::Ctnnb1(ex3)*$^{fl/wt}$ mice by the introduction of floxed *Smarca4* alleles. Unexpectedly, mutated and thereby stabilized β-catenin on its own induced severe developmental phenotypes in male and female *Blbp-cre::Ctnnb1(ex3)*$^{fl/wt}$ mice in our hands, including a thinned cerebral cortex, hydrocephalus, missing cerebellar layering, and cell accumulations in the brainstem and cerebellum. An additional loss of SMARCA4 even resulted in prenatal death for most mice. Respective *Blbp-cre::Ctnnb1(ex3)*$^{fl/wt}$*::Smarca4*$^{fl/rec}$ mutants (male and female) developed large proliferative lesions in the cerebellum evolving from E13.5 to E16.5. Histological and molecular analysis of these lesions by DNA methylation profiling and single-cell RNA sequencing suggested an origin in early undifferentiated SOX2-positive cerebellar progenitors. Furthermore, upregulated WNT signaling, altered actin/cytoskeleton organization, and reduced neuronal differentiation were evident in mutant cells. In vitro, cells harboring alterations in both *Ctnnb1* and *Smarca4* were negatively selected and did not show tumorigenic potential after transplantation in adult female recipient mice. However, in cerebellar explant cultures, mutant cells displayed significantly increased proliferation, suggesting an important role of the embryonic microenvironment in the development of lesions. Altogether, these results represent an important first step toward the unraveling of tumorigenic mechanisms induced by aberrant WNT signaling and SMARCA4 deficiency.

Key words: Blbp; brain tumor development; cerebellum; medulloblastoma; SMARCA4; WNT

Significance Statement

Our study shows the cooperative effects between activated Wingless/Int-1 (WNT) signaling induced by a stabilizing β-catenin mutation and a loss of chromatin remodeler SMARCA4 in driving the development of highly proliferative cerebellar lesions. This observation could have important implications for WNT medulloblastoma patients, who are frequently affected by both alterations with the functional role of *SMARCA4* mutations in tumorigenesis not deciphered so far. Additionally, this work highlights the divergence of mouse phenotypes after brain-specific activation of WNT signaling from previously published studies and proposes potential reasons for varying recombination using the brain lipid binding protein (*Blbp*)-*cre* mouse strain.

Received Aug. 24, 2023; revised Jan. 26, 2024; accepted Jan. 31, 2024.

Author contributions: C.G., Melanie Schoof, D.H., and U.S. designed research; C.G., Melanie Schoof, and D.H. performed research; C.G., Melanie Schoof, and Michael Spohn analyzed data; C.G. wrote the paper.

This work was supported by the Deutsche Krebshilfe, Bonn, Germany (#70113754). Ulrich Schüller was additionally supported by the Fördergemeinschaft Kinderkrebszentrum Hamburg, Germany. We thank Jacqueline Tischendorf, Vanessa Thaden, Margarethe Gregersen, Jessica Prey (University Medical Center Hamburg–Eppendorf, Germany), Gundula Pilnitz-Stolze and Arne Düsedau (Leibniz Institute of Virology, Hamburg, Germany), and Kristin Hartmann (Mouse Pathology Facility, University Medical Center Hamburg–Eppendorf) for their excellent technical support. We thank the diagnostic team at the Institute of Neuropathology for their histological help and the Single Cell Core Facility of the University Medical Center Hamburg–Eppendorf for their support. We thank Dr. Pierre Chambon (IGBMC, Illkirch-Graffenstaden, France) for providing the *Smarca4*$^{fl/fl}$ mouse strain and Dr. Makoto M. Taketo (Kyoto University, Kyoto, Japan) for providing *Ctnnb1(ex3)*$^{fl/fl}$ mice. Finally, we acknowledge the support of the small animal models core facility of the Leibniz Institute of Virology, Hamburg, Germany.

The authors declare no competing financial interests.

Correspondence should be addressed to Ulrich Schüller at u.schueller@uke.de.

https://doi.org/10.1523/JNEUROSCI.1605-23.2024

Introduction

Aberrant activation of Wingless/Int-1 (WNT) signaling is associated with a variety of cancers and is typically induced by mutations in core components of the signaling pathway such as the β-catenin–encoding gene *CTNNB1*. These mutations stabilize β-catenin, which enters the nucleus to drive the expression of WNT targets including MYC and cyclin D1 to promote tumor cell proliferation (Liu et al., 2022). Outside of tumors in the CNS, β-catenin mutations are frequently detected in melanoma, endometrial cancer, hepatocellular carcinoma, and colorectal cancers (Kim and Jeong, 2019). Within brain tumor entities, they are mostly associated with WNT medulloblastoma (MB), occurring in ∼95% of cases (Northcott et al., 2017; Gajjar et al., 2021). WNT is one of the four molecular types of MB that are routinely classified based on their global DNA methylation profile: WNT, sonic hedgehog (SHH), Group 3, and Group 4 (Taylor et al., 2012; Capper et al., 2018). WNT MB show a classic morphology and a very good prognosis with a median 5-year overall survival of 90–100% (Gajjar et al., 2021; Goschzik et al., 2022). However, patients still suffer from long-term treatment-related morbidities, which is why several clinical studies aim at treatment de-escalation with reduced doses of radiation and chemotherapy (Thompson et al., 2020; Mynarek et al., 2021). Meanwhile, targeted therapies for WNT MB are still lacking (Gatto et al., 2022).

The first WNT MB mouse model *Blbp-cre::Ctnnb1(ex3)*$^{fl/wt}$*::Trp53*$^{fl/wt}$ combined a stabilizing mutation in *Ctnnb1* with a loss of tumor suppressor p53, which resulted in tumors originating from progenitor cells of the lower rhombic lip (LRL; Gibson et al., 2010). Later, a comparison of WNT MB transcriptomes to a single-cell transcriptome atlas of the murine and human developing brain more specifically defined pontine mossy fiber neurons as the cells of origin for WNT MB (Jessa et al., 2019). The WNT MB model described by Gibson et al. showed low penetrance (15%) and long latency, which was later amended by an additional introduction of a phosphatidylinositol 3-kinase (*Pik3ca*) mutation, resulting in accelerated tumor development with 100% penetrance (Robinson et al., 2012). However, although mutations of *TP53* or *PIK3CA* occur in WNT MB (both at a frequency of 5–10%), the combination of both alterations is extremely rare (Gajjar and Finlay, 2015; Northcott et al., 2017). In contrast, concurrent mutations of *CTNNB1* and *SMARCA4* are detected in roughly 20% of WNT MB cases (Robinson et al., 2012; Northcott et al., 2017; Gajjar et al., 2021; Goschzik et al., 2022). This co-occurrence of both mutations may indicate a functional interplay between both proteins and might hint toward a tumor-promoting effect of a simultaneous alteration of *CTNNB1* and *SMARCA4*.

SMARCA4 (SWI/SNF related, matrix-associated, actin-dependent regulator of chromatin, subfamily A, member 4; also known as BRG1) is a catalytic subunit of the BAF (BRG1/BRM-associated factor) chromatin remodeling complex, which greatly influences gene expression by altering accessibility of DNA regions for the binding of transcription factors (Clapier et al., 2017; Alfert et al., 2019). Functional SMARCA4 is essential for brain development, and alterations are associated with a wide range of neurodevelopmental diseases (Wieczorek et al., 2013; Bögershausen and Wollnik, 2018). Moreover, deleterious *SMARCA4* mutations can be found throughout several cancer entities, including non-small-cell lung cancer, pancreatic cancer, hepatocellular carcinoma, head and neck cancer, and small-cell carcinoma of the ovary (Ramos et al., 2014; Hodges et al., 2018; Fernando et al., 2020). Within the CNS, biallelic loss of *SMARCA4* is detected in rare cases of atypical/teratoid rhabdoid tumors (ATRT) with dismal prognosis (Hasselblatt et al., 2014; Holdhof et al., 2021b). Meanwhile, *SMARCA4* mutations in MB mostly comprise somatic heterozygous missense mutations, which are suggested to have a dominant-negative effect leading to a loss of function (Hodges et al., 2018; Fernando et al., 2020). Despite the high frequency of *SMARCA4* alterations, their role in WNT MB tumorigenesis has not been deciphered yet. We, therefore, combined a SMARCA4 deficiency with mutated β-catenin in a new *Blbp-cre::Ctnnb1(ex3)*$^{fl/wt}$*::Smarca4*$^{fl/fl}$ mouse model to explore the interactions between aberrant WNT signaling and chromatin remodeling in WNT MB tumorigenesis.

Material and Methods

Transgenic animals. All experimental procedures on animals were approved by the Government of Hamburg, Germany (N113/16, N099/2019) and were performed according to national regulations. Mice were kept on a 12 h dark/light cycle, and water and food were available *ad libitum*. Animals of both sexes were used for experiments. The strain *Smarca4*$^{fl/fl}$ (also known as *Brg1*$^{fl/fl}$) has been previously described and was provided by Dr. Pierre Chambon, IGBMC (Sumi-Ichinose et al., 1997; Indra et al., 2005), *Blbp-cre* mice were obtained from the NCI Mouse Repository (strain #01XM9; Hegedus et al., 2007), and *Ctnnb1(ex3)*$^{fl/wt}$ mice were provided by M. M. Taketo, Kyoto University (Harada et al., 1999). All strains were maintained on a *C57Bl6/J* background. The day of vaginal plug detection in the morning after mating and ovulation was defined as embryonic day 0.5 (E0.5). Postnatal days were counted starting with postnatal day 0 (P0) on the day of birth. Genotyping was performed by PCR using genomic DNA from ear or tail biopsies with the following primer pairs (5′-3′): *cre* (fw): TCCGGGCTGCCACGACCAA, *cre* (rv): GGCGCGGCAACACCATTTT, *Smarca4* floxed (fw): GTC ATACTTATGTCATAGCC, *Smarca4* floxed (rv): GCCTTGTCTCAAAC TGATAAG, *Smarca4* recombined (fw): GATCAGCTCATGCCC TAAGG, *Smarca4* recombined (rv): GCCTTGTCTCAAACTGATAAG, *Ctnnb1(ex3)* floxed (fw): CGTGGACAATGGCTACTCAA, *Ctnnb1(ex3)* floxed (rv): TGTCCAACTCCATCAGGTCA, *Ctnnb1(ex3)* recombined (fw): GTTCTCTTCCCTTCTGCACAC, *Ctnnb1(ex3)* recombined (rv): CTCTGAGCCCTAGTCATTGCATA, *Ctnnb1(ex3)* recombined for formalin-fixed paraffin-embedded (FFPE; fw): ATCACGAGGCCCTTTC GTCT, *Ctnnb1(ex3)* recombined for FFPE (rv): TAGTCATTGCATAC TGCCCGT, red fluorescent protein (*RFP*) floxed (fw): AAAGTCGCTC TGAGTTGTTAT, *RFP* wildtype (rv): GGAGCGGGAGAAATGGATA TG, *RFP* floxed (rv): GCGAAGAGTTTGTCCTCAACC. Cre-negative littermates shown as controls belong to three different genotypes: *Ctnnb1(ex3)*$^{fl/wt}$*:Smarca4*$^{fl/wt}$, *Ctnnb1(ex3)*$^{fl/wt}$*::Smarca4*$^{fl/fl}$ (with cre-positive fathers), and *Ctnnb1(ex3)*$^{fl/wt}$*::Smarca4*$^{fl/rec}$ (with cre-positive mothers). As neither of them showed any phenotype and all mice were viable and healthy at all time points analyzed, we summarized them as cre-negative controls unless otherwise stated in the figure legends.

Immunohistochemistry. For histological examination of brains, tissue was fixed in 4% formaldehyde for at least 12 h. The tissue was dehydrated, embedded in paraffin, and sectioned at 2 µm according to standard protocols. Hematoxylin and eosin (HE) stainings were applied according to standard protocols. DAB stainings were performed on a Ventana BenchMark XT system using the ultraView or OptiView DAB detection kit (Roche Diagnostics). The following antibodies were used: β-catenin (Agilent catalog #M3539; RRID, AB_2086135; 1:100), calbindin (Millipore catalog #AB1778; RRID, AB_2068336; 1:100), cre (BioLegend catalog #908001; RRID, AB_2565079; 1:100), GFAP (Agilent catalog #M0761; RRID, AB_2109952; 1:200), Ki67 (Abcam catalog #ab15580; RRID, AB_443209; 1:100), nestin (Abcam catalog #ab221660; RRID, AB_2909415; 1:2,000), NeuN (Millipore catalog #MAB377; RRID, AB_2298772; 1:50), OLIG2 (Millipore catalog

#AB9610; RRID, AB_570666; 1:200), parvalbumin (Millipore catalog #MAB1572; RRID, AB_2174013; 1:2,000), PAX6 (BioLegend catalog #901301; RRID, AB_2565003; 1:1,000), RFP (Antibodies-Online catalog #ABIN129578; RRID, AB_10781500; 1:50), S100 (Agilent catalog #Z0311; RRID, AB_10013383; 1:100), SMARCA4 (Abcam catalog #ab110641; RRID, AB_10861578; 1:25), and SOX2 (Abcam catalog #ab92494; RRID, AB_10585428; 1:200).

Immunofluorescence (IF) stainings. IF stainings of FFPE tissue were performed manually after deparaffinization and antigen retrieval with citrate buffer. Cytospins were used directly for IF stainings after fixation with 4% formaldehyde. Blocking was performed with 10% NGS in 0.3% Triton X-100. The following primary antibodies were used for incubation at 4°C over night: BrdU (Invitrogen catalog #B35128; RRID, AB_2536432; 1:100); GLUT-1 (Millipore catalog #07-1401; RRID, AB_1587074; 1:500), PAX2 (Thermo Fisher Scientific catalog #71-6000; RRID, AB_2533990; 1:200), pHH3 (Cell Signaling Technology catalog #9706; RRID, AB_331748; 1:200), BLBP (Abcam catalog #ab131137; RRID, AB_11157091; 1:100), and SMARCA4 (Abcam catalog #ab110641; RRID, AB_10861578: 1:25). Secondary antibodies (1:500) and DAPI (1 µg/ml) were added for 1 h at room temperature on the next day: anti-mouse Alexa 488 (Cell Signaling Technology catalog #4408; RRID, AB_10694704), anti-mouse Alexa 555 (Cell Signaling Technology catalog #4409; RRID, AB_1904022), anti-rabbit Alexa 488 (Cell Signaling Technology catalog #4412; RRID, AB_1904025), and anti-rabbit Alexa 546 (Thermo Fisher Scientific catalog #A-11035; RRID, AB_2534093).

Image analysis and quantification. All immunohistochemistry (IHC) and HE stainings were imaged using the Olympus BX43 brightfield microscope and the Olympus cellSens software (Olympus). For imaging of IF stainings, the Nikon Ti2 microscope with the camera DS Qi2 and the corresponding software NIS-Elements (v5.11.03) was used (Nikon). White balance correction of brightfield images was performed using the GIMP image manipulation software (v2.10.28, freeware at www.gimp.org).

Quantification of areas in IHC was performed with ImageJ (v1.53). Total brain area and cerebellar area were measured with the *Measure* tool using HE-stained sagittal sections of comparable brain layers. Area measurement of the Ki67-positive area on IHC slides was performed after cropping pictures to display a region of 200 µm in height measured from the fourth ventricle. Then, images were converted into 8-bit format, and the same black/white threshold was applied to all pictures analyzed. The tools *Erode*, *Dilate*, and *Remove Outliers* were used to optimize the mask before applying the *area_fraction* tool to measure the fraction of the white area corresponding to a positive Ki67 signal.

To determine the percentage of labeled cells in IF stainings, the *Automatic Measurement* tool of the NIS-Elements software (v5.11.03, Nikon) was used. The threshold for fluorescence intensity and cell size was adjusted separately for each fluorescence channel and was applied to all samples to retrieve cell counts. At least three representative images were analyzed for each sample and staining. When big piles of cells were present within pictures, single cells were separated manually within these regions. Binary levels were created to analyze the overlay of two different fluorescent channels.

DNA methylation analysis. DNA isolation from FFPE punch biopsies was performed using the Maxwell RSC DNA FFPE kit (Promega). At least 150 ng of total DNA was used for bisulfite conversion with the EZ DNA methylation kit (Zymo Research). Then, samples were analyzed on the Infinium Mouse Methylation BeadChip array covering >285,000 CpG sites within the mouse genome on an iScan array scanner (Illumina). Human tumor samples were analyzed on the MethylationEPIC 850 k BeadChip array (Illumina). The use of biopsy specimens for research upon anonymization was always in accordance with local ethical standards and regulations at the University Medical Center Hamburg–Eppendorf.

Data processing and analysis was performed with R (v4.1.2). For a comparison of methylation profiles between mouse samples only, samples were preprocessed with *SeSaMe* (Zhou et al., 2018) and quantile normalized. Principal component analysis (PCA) was performed with the *prcomp* function using the 10,000 most differentially methylated CpG sites. Overrepresentation analysis (ORA) was applied using the *methylGSA* package with *methylRRA* adjustment (Ren and Kuan, 2019) with user-supplied mapping between CpG ID and gene name in the mouse genome. Gene ontology (GO) terms associated with biological processes were summarized and visualized with REVIGO (Supek et al., 2011). The resulting interactive graph was further adjusted using the Cytoscape software v3.9.1 (Shannon et al., 2003).

For a comparison of murine samples to human brain tumors, previously published data (Capper et al., 2018; Sharma et al., 2019) were combined with data generated in-house (in total $n = 1{,}683$). Preprocessing of raw data was performed with the *Minfi* package (Aryee et al., 2014) for human data, whereas the *SeSaMe* package was used for mouse data as described above. Then, quantile normalization of data was performed. Within the human dataset, the 15,000 most differentially methylated CpG sites were identified. Out of these, 491 CpGs that are orthologous between the human and mouse genome were chosen for further analysis. Human and mouse datasets were combined, and again, quantile normalization was performed. Uniform Manifold Approximation and Projection for Dimension Reduction (UMAP; McInnes et al., 2018) and hierarchically clustered heatmaps (*Complex Heatmap* package; Gu et al., 2016) were generated based on the differential methylation of the previously chosen 491 CpGs.

Culture of hindbrain progenitor cells. For the isolation of hindbrain progenitor cells (HPCs), E14.5 embryos (*Blbp-cre::Ctnnb1(ex3)*$^{fl/wt}$*::Smarca4*$^{fl/rec}$, *Blbp-cre::Ctnnb1(ex3)*$^{fl/wt}$*::Smarca4*$^{fl/wt}$, or cre-negative littermates) were collected by cesarean section and were killed by decapitation. Hindbrains were dissected under a dissecting microscope (Leica M165 FC, Leica Camera) and were digested in papain/DNase solution (papain, 20 U/ml; DNase, 400 µg/ml) at 37°C for 30–60 min. Singularized cells were transferred into T25 flasks in neural stem cell (NSC) medium (DMEM/F-12 + GlutaMAX, 40 mM HEPES, 1× B27 supplement, 1× MEM non-essential amino acid solution, 50 U/ml Pen-Strep, 20 ng/ml EGF, 20 ng/ml FGF) to form neurospheres in suspension cultures. EGF and FGF were freshly added every 2–3 d during the cultivation period. Every week, neurospheres were singularized using Accutase, and cells were counted and reseeded into new T25 flasks at 1 mio cell per flask. Population doublings (PD) were then calculated as follows: $PD = \log_2$ (cell count/cells seeded). To fix HPC neurospheres on cytospins for stainings, $\sim 5 \times 10^5$ cells were resuspended in PBS and centrifuged at 500 rpm with low acceleration for 5 min in a Cytospin 4 centrifuge (Thermo Fisher Scientific). Then, cells were fixed by applying 4% formaldehyde for 20 min. For adherent cell cultures, HPCs were singularized and seeded onto poly-L-ornithine (PLO) coated 24-well plates (15 µg/ml) at a density of 200,000 cells per well.

Transplantation of HPCs. Transplantation of HPCs was performed directly after isolation and cell counting. The cell pellet was washed in 50 µl of cold NSC medium, transferred into a new tube, and resuspended in 4 µl of 3:1 NSC medium with Matrigel (Growth Factor Reduced). Cells were kept on ice until ready for injection. During stereotactic transplantations, recipient mice (6-week-old *CD1*$^{nu/nu}$) were anesthetized by isoflurane inhalation. They additionally received analgesia by subcutaneous injections of carprofen (6 mg/kg) before transplantation and on the day after. For the procedure, mice were placed in a stereotactic frame (David Kopf Instruments) on a heating pad, and eye ointment was applied to avoid dehydration. Local anesthesia (2% lidocaine) was applied before performing a skin incision and puncturing the skull for injection. Total HPCs derived from one embryonal hindbrain each were injected using a Hamilton syringe (World Precision Instruments) at coordinates x, +1 mm; y, −1 mm; and z, −2 mm from the lambda suture at 30° from the skull surface. Mice were monitored daily for any sign of tumor development within the following 6 months.

Cerebellar explants. For explant cultures, cerebella of E14.5 embryos were dissected, minced with a scalpel, and transferred into 24-well plates

coated with PLO (15 µg/ml) and laminin (20 µg/ml). They were cultured in an NSC medium supplied with EGF and FGF as described for the HPC culture above.

Single-cell gene expression analysis. Single-cell RNA sequencing was performed using HPCs from E16.5 embryos isolated as described above. Three controls (cre-negative littermates) and three mutants (*Blbp-cre::Ctnnb1(ex3)$^{fl/wt}$::Smarca4$^{fl/rec}$*) were chosen for further processing, and living cells were sorted by excluding dead 7-aminoactinomycin D–positive cells using a BD FACSAria fusion flow cytometer (BD Biosciences). Before starting library preparation, samples were pooled together in similar quantities to generate one control and one mutant sample. Preparation of single-cell gene expression libraries was performed at the Single Cell Core Facility of the University Medical Center Hamburg using the Chromium Next GEM Single Cell 3′ v3.1 kit (10x Genomics) with 40,000 cells of each pooled sample. The sufficient quality of the generated library was confirmed on a TapeStation with the High Sensitivity D5000 ScreenTape (Agilent). Paired-end sequencing of libraries was performed at Novogene UK on a NovaSeq 6000 sequencing system (Illumina).

Raw sequencing reads were aligned against a murine reference genome (*mm10-2020-A*, provided by 10x Genomics) and were simultaneously counted with the *Cell Ranger* pipeline (v7.0.1; Zheng et al., 2017) employing the count command. The output from *Cell Ranger* was loaded into *R* (v4.1.1) via the *Seurat* package (v4.0.5; Hao et al., 2021), including only genes expressed in a minimum of three cells and cells expressing a minimum of 200 features. Control and mutant datasets were merged and further filtered to include only cells expressing >1,500 and <7,500 features, <5% mitochondrial genes, and <40,000 overall reads. The merged dataset was then normalized and scaled, and the PCA was calculated based on the 2,000 most variable genes. The first 50 dimensions and a resolution of 0.5 were chosen for UMAP and clustering. To annotate cell classes and subclasses in the resulting clusters, a label transfer method based on Stuart et al. (2019) was chosen using a murine reference dataset (La Manno et al., 2021). Briefly, anchor cells between the query dataset and reference are chosen in low dimensional PCA space, and labels are transferred by a weights matrix that defines the association between the query cells and the anchor cells and a binary matrix of the label and the anchor cells. Similarly, the age of cells was predicted using the La Manno et al. (2021) dataset from E10.0 to E16.5 as a reference. The following modifications were performed for predicted subclasses: exclusion of subclasses with <10 cells; summary of "meninges" (Pia1/2/3, intermediate meninges, dura, arachnoid); summary of "microglia" (axon tract-associated microglia, cycling microglia, noncycling microglia); and undefined cells with prediction class "blood" also defined as "blood" in subclasses. Cell cycle scores were assigned using the *CellCycleScoring* tool in *Seurat*. To determine differentially expressed genes (DEGs) between two sets of cells, a fold change of the average expression values plus a pseudocount of one was calculated, and a Wilcoxon rank sum test was performed. The resulting *p*-value was Bonferroni corrected, and a gene was called a DEG with |average log2 fold change| > 1 and adjusted $p < 0.01$. GSEA was performed using the *fgsea* (v1.20.0) *R*-package with the category *WIKIPATHWAYS* chosen from *MsigDB* via the *msigdbr* (v7.5.1) *R*-package. Gene lists ranked by average log2Foldchange were used as input and the lower bound for *p*-value calculation was set to zero. To infer the development of different brain cell types, a trajectory analysis by the *monocle R*-package (v2.2.0) was applied to cells originating from the mutant sample. Again, DEGs were estimated, but this time employing *monocle*'s inherent *differentialGeneTest* function between the beforehand assigned cell types. After reducing dimensions to two by the *DDRTree* method, the cells were ordered by DEGs with $q < 0.01$, and trajectory was estimated in the reduced dimensional space. Lastly, we examined RNA velocity with *Python* (v3.6.8) and the corresponding package *scVelo* (v0.2.5). Visualizations are based on UMAP embeddings imported from *Seurat*.

Experimental design and statistical analysis. All statistical analysis was performed using the GraphPad Prism (v9.4.1) or R (v4.1.2) software. The statistical tests applied to the data shown are stated in the respective text passages within the results. For each comparison, at least $n = 3$ samples per group were used, and/or $n = 3$ independent experiments were conducted. When comparing two groups only, two-tailed unpaired Welch's *t* test or, in the case of paired data, two-tailed paired *t* tests were performed. For comparisons between more than two groups, Tukey's multiple-comparisons tests after ANOVA were applied. Dunnett's multiple-comparisons test after ANOVA was applied when comparing means to a control group only. To determine DEGs in single-cell RNA sequencing, the Wilcoxon rank sum test with Bonferroni's correction was applied. The chi-square test was applied when comparing expected versus counted values in mouse breeding. *p* values were corrected for multiple testing whenever more than two groups were compared. All graphs depict mean ± SD.

Results

Severe developmental phenotypes and early lethality of *Blbp-cre::Ctnnb1(ex3)$^{fl/wt}$* mice

In the first step, we analyzed postnatal mice harboring mutated β-catenin, SMARCA4 loss, or a combination of both alterations under the control of the *Blbp* promoter. *Blbp-cre::Ctnnb1(ex3)$^{fl/wt}$* mice developed a severe neurodevelopmental phenotype with a median survival of only 2 d (Fig. 1*A*). All mice were either found dead shortly after birth ($n = 10$) or had to be killed due to ataxia and hydrocephalus within the first 3 weeks of life ($n = 8$). This was unexpected since this phenotype had not been described before for *Blbp-cre::Ctnnb1(ex3)$^{fl/wt}$* mice (Gibson et al., 2010). An additional heterozygous loss of SMARCA4 in *Blbp-cre::Ctnnb1(ex3)$^{fl/wt}$::Smarca4$^{fl/wt}$* mice did not influence observed phenotypes or survival (median survival, 2.5 d). In contrast, mice bearing a homozygous loss of SMARCA4 alone (*Blbp-cre::Smarca4$^{fl/fl}$*) died even earlier (median survival, <1 d). Only one mouse survived until P11 when it had to be killed due to severe ataxia. Lastly, combined mutation of β-catenin and homozygous SMARCA4 loss in *Blbp-cre::Ctnnb1(ex3)$^{fl/wt}$::Smarca4$^{fl/fl}$* mice resulted in the highest lethality. All mice born with this genotype were either found dead at birth or died on the same day ($n = 8$). *Blbp-cre::Smarca4$^{fl/wt}$* mice did not show any phenotype and were treated as equivalent to controls in further investigations.

Blbp-cre::Ctnnb1(ex3)$^{fl/wt}$ and *Blbp-cre::Ctnnb1(ex3)$^{fl/wt}$::Smarca4$^{fl/wt}$* mice that survived up until P15 showed macroscopic hydrocephalus and were smaller compared with cre-negative controls (littermates; Fig. 1*B*). Their weight was significantly reduced in comparison with controls within their second week of life (Fig. 1*C*, $^{**}p \leq 0.01$, $^{***}p \leq 0.001$, $^{****}p \leq 0.0001$, Dunnett's multiple comparisons). Histologically, both genotypes showed a severe hydrocephalus and hypoplastic cerebella with significantly reduced sizes in comparison with controls ($F_{(2,9)} = 25.72$, $p = 0.0002$, ANOVA; adjusted $p = 0.001/p = 0.0002$, Tukey's multiple comparisons, Fig. 1*D–G*). The cerebellum of mutants showed severe architectural abnormalities with disturbed layering and cell accumulations in both the cerebellum and dorsal brainstem (Fig. 1*H–P*). IHC stainings revealed nuclear accumulation of β-catenin in cellular accumulations of both regions and both mutants, while partial SMARCA4 loss was only visible in cell accumulations of *Blbp-cre::Ctnnb1(ex3)$^{fl/wt}$::Smarca4$^{fl/wt}$* mice (Fig. 1*Q–B′*). Altogether, proliferation as indicated by Ki67 expression was very low in all cell accumulations detected, pointing toward a neurodevelopmental phenotype rather than tumorous lesions (Fig. 1*C′–H′*). Both accumulations in brainstem and cerebellum of *Blbp-cre::Ctnnb1(ex3)$^{fl/wt}$* mice showed similar patterns in IHC by staining positive for cre, nestin, and SOX2 with sparse expression of GFAP and OLIG2 and

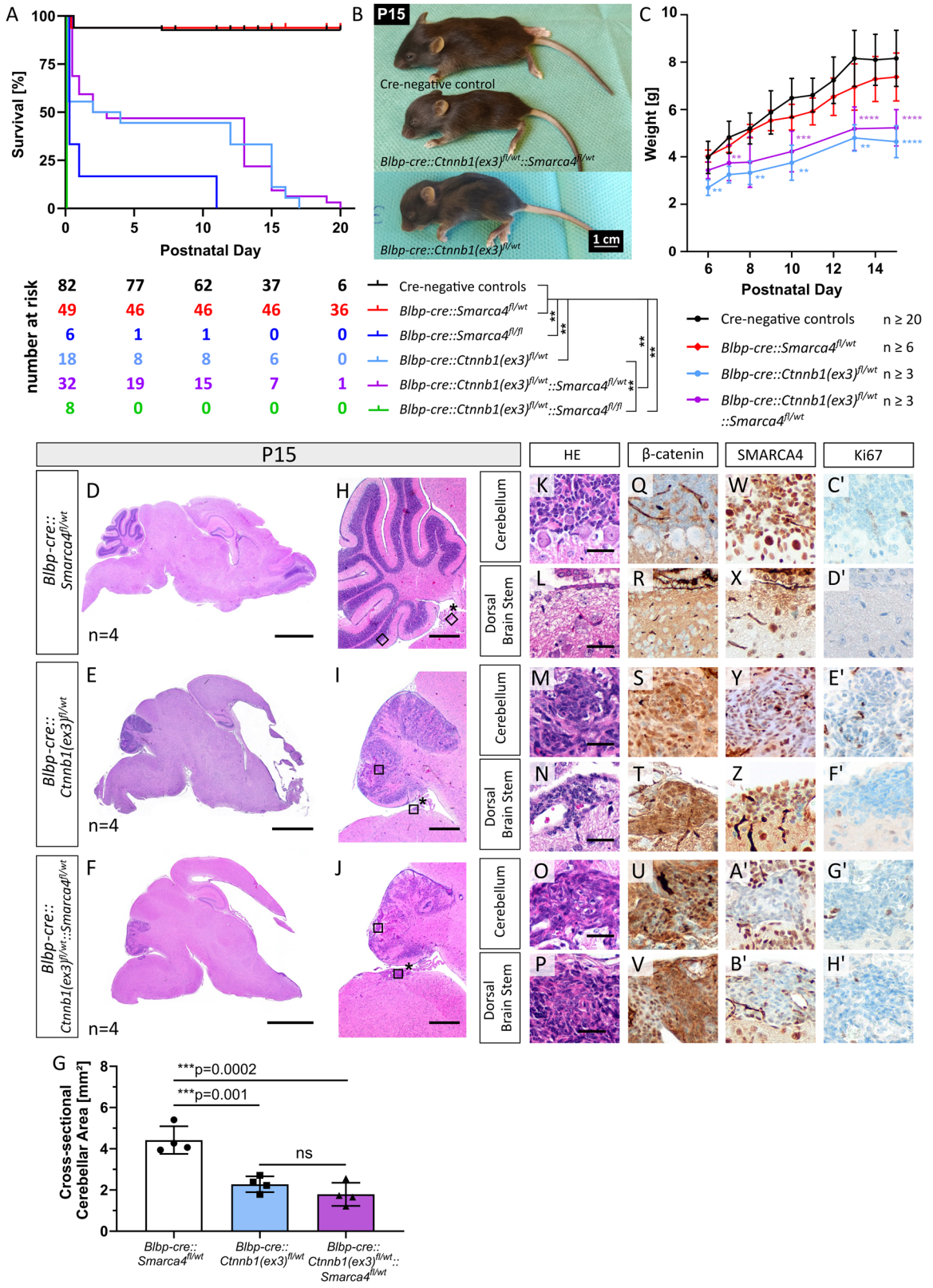

Figure 1. Continued.

no signal for parvalbumin, PAX6, S100, NeuN, and calbindin, suggesting an origin in undifferentiated neural progenitor cells (Fig. 2*A–J′*).

To find an explanation for the unexpected severity of phenotypes in our breeding of *Blbp-cre::Ctnnb1(ex3)*$^{fl/wt}$ mice, we generated fate-mapping mice to track the expression of BLBP. Staining of RFP in *Blbp-cre::IsIR26tdRFP*$^{fl/wt}$ mice at embryonic day 14.5 (E14.5) revealed broad expression throughout the whole developing cerebellum, the brainstem, and parts of the midbrain and rostral cerebral cortex (Fig. 3*A–F*). This pattern of RFP expression correlates with BLBP expression, although the expression of RFP is visible in more cells. This is due to the fact that BLBP staining marks all cells expressing BLBP at E14.5, whereas RFP is expressed in all cells that have expressed BLBP since its onset of expression at E9.5 (Fig. 3*G–I*). In contrast, Gibson et al. previously showed recombination by *Blbp-cre* at the same developmental stage mostly restricted to the germinal zones of the cerebellum (LRL, upper rhombic lip [URL], ventricular zone [VZ], external granular layer; Gibson et al., 2010).

An analysis of mutants at birth (P0) revealed that the phenotype of *Blbp-cre::Ctnnb1(ex3)*$^{fl/wt}$ mice with severe hydrocephalus and dorsal brainstem lesions was already evident at this point in time (Fig. 4*A–T*). Additionally, mice displayed lesions in the cerebral cortex at this stage. At the same time, *Blbp-cre::Smarca4*$^{fl/fl}$ mice developed a hydrocephalus and a hypoplastic cerebellum while showing a loss of SMARCA4 but no aberrant cell accumulations in either the brainstem or cerebral cortex (Fig. 4*U–D′*). *Blbp-cre::Ctnnb1(ex3)*$^{fl/wt}$*::Smarca4*$^{fl/fl}$ mice displayed hydrocephalus and severely hypoplastic cerebellum and showed no signs of tumor development (Fig. 4*E′–N′*). However, counted versus expected genotypes in our breeding revealed that both mutants *Blbp-cre::Smarca4*$^{fl/fl}$ and *Blbp-cre::Ctnnb1(ex3)*$^{fl/wt}$*::Smarca4*$^{fl/fl}$ were born at a highly reduced frequency relative to expected Mendelian ratio, with 22% and 26% of expected mice born, respectively (chi-square = 63.07, DF = 5, $p < 0.0001$, Fig. 4*O′*). These values suggested prenatal lethality of both mutant genotypes and prompted us to additionally analyze mice at the embryonic stage.

Blbp-cre::Ctnnb1(ex3)$^{fl/wt}$*::Smarca4*$^{fl/rec}$ mice develop proliferative cerebellar lesions at embryonic age

Blbp-cre::Ctnnb1(ex3)$^{fl/wt}$*::Smarca4*$^{fl/rec}$ mice (further referred to as "mutants") displayed big cerebellar lesions in the developing cerebellum at E14.5 that were not visible in cre-negative controls (Fig. 5*A–D*). Lesions were mainly located within the two developing cerebellar hemispheres (Fig. 5*E–H*). They were cell dense, were interspersed with blood vessels, and showed nuclear accumulation of β-catenin and a loss of SMARCA4 in all cells (Fig. 5*I–N*). Furthermore, they expressed Cre and stained positive for SOX2, the expression of which is usually restricted to the VZ (Fig. 5*O,P,R,S*). Proliferation as measured by Ki67-positive area was significantly increased in mutants compared with the corresponding region in controls ($t = 5.036$, DF = 4.314, $p = 0.0060$, Welch's *t* test; Fig. 5*Q,T–U*). Additionally, lesions often displayed rosette-like features, a characteristic attributed to neural stem cells, and a phenomenon also occurring in some MB cases (Wilson and Stice, 2006; Orr, 2020; Fig. 5*V–W*). The adjustment of the mutant genotype *Blbp-cre::Ctnnb1(ex3)*$^{fl/wt}$*::Smarca4*$^{fl/fl}$ to *Blbp-cre::Ctnnb1(ex3)*$^{fl/wt}$*::Smarca4*$^{fl/rec}$ was caused by our finding of *Smarca4* germline recombination in the offspring of cre-positive mothers, which strongly influenced phenotypes. While 12 of 13 mutants derived from breeding with cre-positive mothers (*Blbp-cre::Smarca4*$^{fl/wt}$ females crossed with *Ctnnb1(ex3)*$^{fl/fl}$*::Smarca4*$^{fl/fl}$ males) displayed cerebellar lesions at E14.5, 0 of 5 mutants derived from cre-positive fathers (*Blbp-cre::Smarca4*$^{fl/wt}$ males crossed with *Ctnnb1(ex3)*$^{fl/fl}$*::Smarca4*$^{fl/fl}$ females) developed cerebellar lesions (three litters analyzed). Consequently, we investigated *Smarca4* recombination in embryonic tail biopsies to test for germline recombination since BLBP is not physiologically expressed in this region. PCR analysis revealed a recombined *Smarca4* allele in the tails of all *Blbp-cre::Ctnnb1(ex3)*$^{fl/wt}$*::Smarca4*$^{fl/rec}$ and *Ctnnb1(ex3)*$^{fl/wt}$*::Smarca4*$^{fl/rec}$ offspring derived from cre-positive mothers (Extended Data Table 5-1). The fact that recombination was independent of the cre status of the embryos themselves suggested that *Smarca4* recombination had already occurred in the oocytes of mothers (Hayashi et al., 2003; Luo et al., 2020). In contrast, none of the embryos derived from cre-positive fathers showed germline recombination of *Smarca4* (Fig. 5*X*, breeding scheme). The parents themselves were not chimeras for *Smarca4* recombination as tested in multiple tissues (Extended Data Table 5-1). Furthermore, recombined *Ctnnb1* alleles were never found in tail biopsies of embryos derived from cre-positive mothers. We concluded that the preceding loss of one *Smarca4* allele in the germline before the cre-induced loss of the second *Smarca4* allele and cre-induced mutation of *Ctnnb1* greatly influences observed phenotypes in mutants. Therefore, we decided to perform all the following analyses with offspring of cre-positive mothers only.

We further characterized cerebellar lesions in *Blbp-cre::Ctnnb1(ex3)*$^{fl/wt}$*::Smarca4*$^{fl/rec}$ mutants by IF costaining of SMARCA4 and mitotic marker phosphohistone H3 (pHH3; Fig. 6*A–H*). While cell density was not significantly increased in the lesions (Fig. 6*E*; $t = 1.341$, DF = 5.055, $p = 0.2371$, Welch's *t* test), SMARCA4 knockdown was visible in ∼90% of cells (Fig. 6*F*; $t = 76.49$, DF = 4, $p < 0.0001$, one-sample *t* test). The mitotic cell count was significantly increased in the lesions compared with controls (Fig. 6*G*; $t = 3.167$, DF = 5.224, $p = 0.0234$, Welch's *t* test) with significantly more SMARCA4-negative mitotic cells than SMARCA4-positive mitotic cells (Fig. 6*H*; $t = 4.821$, DF = 4, $p = 0.0085$, paired *t* test). Next, we had a closer look at cell populations within the cerebellar VZ, where the lesions seemed to originate.

←

Figure 1. Early lethality and severe developmental phenotypes of *Blbp-cre::Ctnnb1(ex3)*$^{fl/wt}$ mice. ***A***, Survival curves of different mouse genotypes stated in the legend beneath. All *Blbp-cre::Ctnnb1(ex3)*$^{fl/wt}$*::Smarca4*$^{fl/fl}$ mutants died at birth or within the first day of life. The table beneath the graph depicts numbers at risk for the respective genotypes and postnatal days. Log-rank tests with Bonferroni's correction were performed (see detailed statistical values in Extended Data Table 1-1). ***B***, Macroscopic hydrocephalus and reduced size of mutant mice at sacrifice (P15). ***C***, Significantly reduced weight of mutant mice compared with controls within the second week of life (**$p \leq 0.01$, ***$p \leq 0.001$, ****$p \leq 0.0001$, see detailed statistical values and *n* values for each comparison in Extended Data Table 1-1). ***D–F***, HE staining of sagittal brain sections reveals hydrocephalus and hypoplastic cerebella in *Blbp-cre::Ctnnb1(ex3)*$^{fl/wt}$ and *Blbp-cre::Ctnnb1(ex3)*$^{fl/wt}$*::Smarca4*$^{fl/wt}$ mice compared with *Blbp-cre::Smarca4*$^{fl/wt}$ controls. The asterisk indicates the location where hindbrain lesions develop in mutant animals. ***G***, Cross-sectional cerebellar area is significantly reduced in mutants as measured in HE sagittal sections of four mice each. ***H–J***, HE stainings show defective lamination and foliation in the cerebella of both *Blbp-cre::Ctnnb1(ex3)*$^{fl/wt}$ and *Blbp-cre::Ctnnb1(ex3)*$^{fl/wt}$*::Smarca4*$^{fl/wt}$ mice. ***K–H′***, HE and IHC of aberrant cell accumulations in the cerebellum and dorsal brainstem of mutants (corresponding to black rectangles in ***H–J*** with and without asterisks, respectively). Cell accumulations show nuclear accumulation of β-catenin (***S***, ***T***, ***U***, ***V***), partial loss of SMARCA4 only in *Blbp-cre::Ctnnb1(ex3)*$^{fl/wt}$*::Smarca4*$^{fl/wt}$ mutants (***A′***, ***B′***), and weak proliferation in both mutants at both locations (***E′–H′***). Scale bars in ***D*** and ***E***, and ***F*** correspond to 2 mm; in ***H***, ***I***, and ***J*** to 500 µm; and in ***K–P*** to 50 µm (also applicable to panels ***Q–H′***).

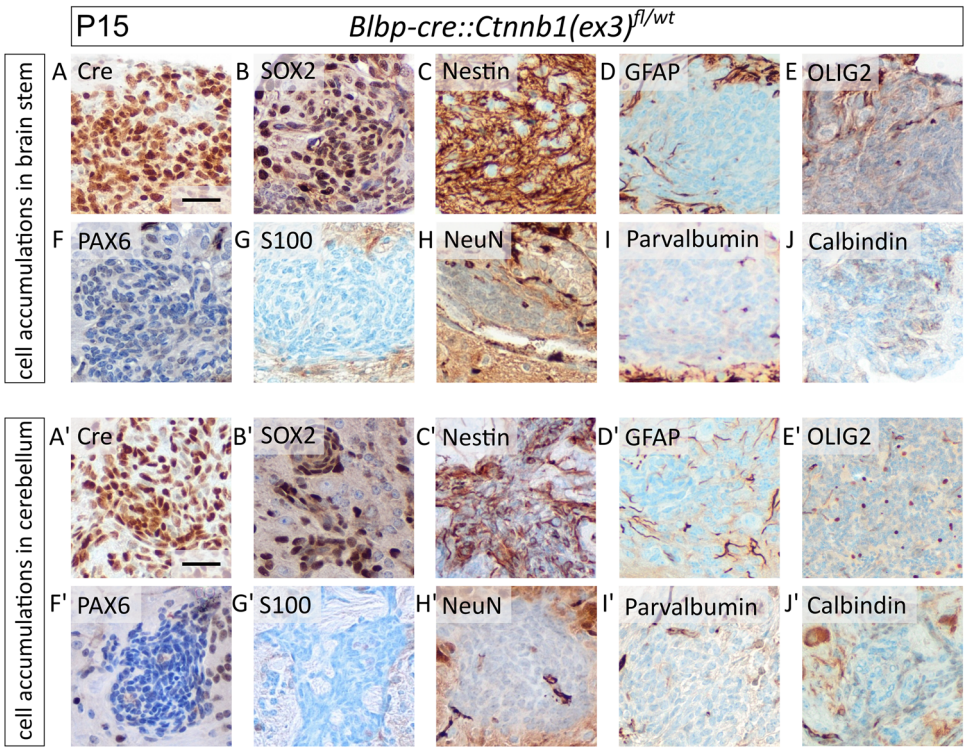

Figure 2. Histological characterization of cell accumulations in the cerebellum and brainstem of *Blbp-cre::Ctnnb1(ex3)*$^{fl/wt}$ mutants. Cell accumulations in both locations at P15 display similar immunohistochemistry, staining positive for Cre (***A***, ***A′***), SOX2 (***B***, ***B′***), and nestin (***C***, ***C′***) with sparse to no expression of GFAP (***D***, ***D′***) and OLIG2 (***E***, ***E′***) and negativity for PAX6 (***F***, ***F′***), S100 (***G***, ***G′***), NeuN (***H***, ***H′***), parvalbumin (***I***, ***I′***), and calbindin (***J***, ***J′***). Scale bars in ***A***, ***A′*** correspond to 50 µm and are applicable to all remaining panels.

During embryonic hindbrain development, the cerebellar VZ gives rise to PAX2-positive inhibitory interneurons, which migrate radially inside the cerebellum from E12.5 on (Seto et al., 2014). While migrating PAX2-positive precursors were visible in controls at E14.5, they were not detected throughout the whole mutant cerebellum, suggesting disturbed differentiation toward this lineage in mutants (Fig. 6*I–L*). Furthermore, we stained for GLUT-1 in blood vessels, which is needed to facilitate glucose transport across the blood–brain barrier (Pardridge et al., 1990; Dermietzel et al., 1992). Phoenix et al. have shown the absence of GLUT-1 in human WNT MB and brainstem lesions of *Blbp-cre::Ctnnb1(ex3)*$^{fl/wt}$*::Trp53*$^{fl/fl}$ mice that both display a defective blood–brain barrier (Phoenix et al., 2016). However, blood vessels in cerebellar lesions of our mutants stained positive for GLUT-1, suggesting a maintained blood–brain barrier in our model (Fig. 6*M–P*). The lesions also expressed BLBP, which is expressed only in the VZ in the controls (Fig. 6*Q-T*). The BLBP expression aligns well with the expression of Cre in the lesions shown in Figure 5*R*.

In addition to *Blbp-cre::Ctnnb1(ex3)*$^{fl/wt}$*::Smarca4*$^{fl/rec}$ mutants described above, we also analyzed other mutant genotypes at E14.5, none of which developed any proliferative cerebellar lesions (Fig. 7*A–H*). *Blbp-cre::Ctnnb1(ex3)*$^{fl/wt}$ and *Blbp-cre::Ctnnb1(ex3)*$^{fl/wt}$*::Smarca4*$^{fl/wt}$ mice had not developed any hindbrain phenotype yet, whereas *Blbp-cre::Smarca4*$^{fl/rec}$ mice showed a partial loss of SMARCA4 in the VZ (Fig. 7*I–T*). The phenotype of *Blbp-cre::Ctnnb1(ex3)*$^{fl/wt}$*::Smarca4*$^{fl/fl}$ mutants derived from cre-positive fathers was similar to *Blbp-cre::Smarca4*$^{fl/rec}$ mutants without any evidence of proliferative lesions (Fig. 7*U–X*).

Cerebellar lesions develop from E13.5 to E16.5

To find out more about the origin and developmental window of the embryonic cerebellar lesions, we analyzed *Blbp-cre::Ctnnb1(ex3)*$^{fl/wt}$*::Smarca4*$^{fl/rec}$ mutants at different embryonic time points (E12.5, E13.5, E14.5, E16.5, E18.5). Cerebellar lesions were detected earliest at E13.5 and expanded until E16.5, at which point they spanned great parts of the developing cerebellum (Fig. 8*A–D*). Although the loss of SMARCA4 was already visible in the cerebella of mutant mice at E12.5, accumulation of β-catenin was not detected yet (Fig. 8*E,F*). From E13.5 on, lesions with a complete loss of SMARCA4 and nuclear accumulation of β-catenin were evident (Fig. 8*G–L*). In contrast, E18.5 and P0 mutants were only found at highly reduced frequencies without displaying any cerebellar lesions (Fig. 8*M*). Histologically, the few mutants found and analyzed at E18.5 or P0 showed a complete loss of SMARCA4 in the cerebellum, whereas nuclear accumulation of β-catenin was not visible (Fig. 8*N-S*). To find an explanation for this discrepancy between phenotypes, we investigated the recombination of *Smarca4* in the germline as well as the local recombination of *Smarca4* and *Ctnnb1* in FFPE brain sections of the mutants histologically analyzed from E12.5 to P0. Germline recombination of *Smarca4* was detected in all mutants including mice without lesions at P0 (Fig. 8*T*). Furthermore, the recombination of *Smarca4* in the brains at P0 was confirmed using DNA extracted from FFPE sections (Fig. 8*U*). However, recombination of *Ctnnb1* was not detected in P0 brains compared with mutants at E14.5 or E16.5, indicating incomplete recombination as a possible cause for the missing lesions and prolonged survival of a few mutants (Fig. 8*V*).

Brainstem cell accumulations do not develop after SMARCA4 loss

A detailed comparison of brains at E16.5 revealed that the cell accumulations in the dorsal brainstem previously detected in

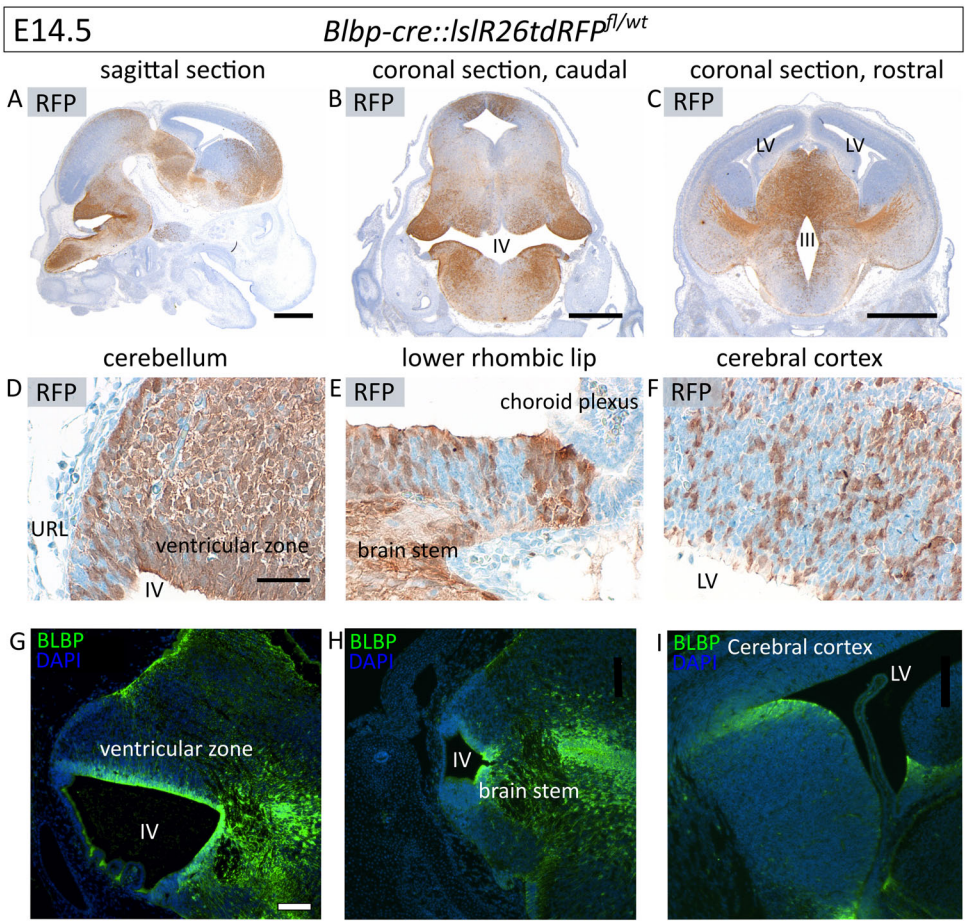

Figure 3. Fate-mapping mice show broad recombination by *Blbp-cre* throughout the embryonic brain. ***A***, RFP staining of *Blbp-cre::lslR26tdRFP*$^{fl/wt}$ embryos at E14.5 (sagittal section of whole head) reveals recombination in the cerebellum, midbrain, and cortex, which was also verified in coronal sections (***B***, ***C***). ***D–F***, High-power images show positive stainings throughout the whole cerebellum (***D***), no signal in the choroid plexus (***E***), and scattered expression in the dorsal brainstem (***E***) and rostral part of the cerebral cortex (***F***). ***G–I***, BLBP expression corresponds to RFP expression but is more restricted in all analyzed tissues. Scale bars in ***A–C*** correspond to 500 µm, and scale bar in ***D*** corresponds to 50 µm and is applicable to ***E–I***. LV = lateral ventricle, III = third ventricle, IV = fourth ventricle, URL = upper rhombic lip.

Blbp-cre::Ctnnb1(ex3)$^{fl/wt}$ mice at P15 and P0 were already visible at this age (Fig. 9*A–L*). In contrast, none of the *Blbp-cre::Ctnnb1(ex3)*$^{fl/wt}$*::Smarca4*$^{fl/rec}$ mutants with cerebellar lesions developed any aberrant accumulations in the brainstem but only showed a loss of SMARCA4 in this region (Fig. 9*M–R*). Brainstem lesions were already described as missing in *Blbp-cre::Ctnnb1(ex3)*$^{fl/wt}$*::Smarca4*$^{fl/fl}$ mutants at P0 (Fig. 4). However, in this case, the presence of cerebellar lesions at E16.5 proved successful *Ctnnb1* recombination in mutants. Consequently, missing cell accumulations are either attributed to insufficient recombination of *Ctnnb1* only in the brainstem region or to the SMARCA4 loss in this region.

Cerebellar lesions show deregulated global DNA methylation

To characterize cerebellar lesions of *Blbp-cre::Ctnnb1(ex3)*$^{fl/wt}$*::Smarca4*$^{fl/rec}$ mutants on a molecular level, we isolated DNA from FFPE punches of control and mutant cerebella at E16.5. Subsequent global DNA methylation analysis was performed using the Mouse Methylation BeadChip (Illumina). PCA based on the 10,000 most differentially methylated CpG sites showed a clear separation of control and mutant samples (Fig. 10*A*). ORA revealed the top 25 differentially methylated gene sets associated with neural development, GTPase activity, cytoskeleton organization, transmembrane transport, and β-catenin binding, providing further evidence for aberrant WNT signaling in the mutants (Fig. 10*B*). Moreover, all significantly differentially methylated GO terms designated as "biological processes" were summarized by REVIGO (Supek et al., 2011) and showed similar trends. Differential DNA methylation was detected within gene sets involved in nervous system development, signal transduction, actin/cytoskeleton organization, and transmembrane transport with a high degree of connectivity (Fig. 10*C*). Additionally, GO terms associated with protein phosphorylation, cell migration, and proliferation and apoptosis were identified.

To compare the methylation profile of murine cerebellar lesions to human brain tumors, we integrated our data with a brain tumor dataset comprising in-house analyzed samples and previously published cohorts (Capper et al., 2018; Sharma et al., 2019). Differential methylation of 491 orthologous CpG sites efficiently separated human tumor subtypes in both UMAP and Euclidian clustering (Fig. 10*D–E*). However, integration of our murine cerebellar lesions yielded non-conclusive results with proximity to ATRTs in UMAP and to spinal paraganglioma in Euclidian clustering (Fig. 10*D–E*).

Single-cell gene expression analysis of cerebellar lesions reveals an undifferentiated nature and upregulation of WNT targets in mutant clusters

To further characterize mutant cell populations in the cerebellum of *Blbp-cre::Ctnnb1(ex3)*$^{fl/wt}$*::Smarca4*$^{fl/rec}$ mice, we performed

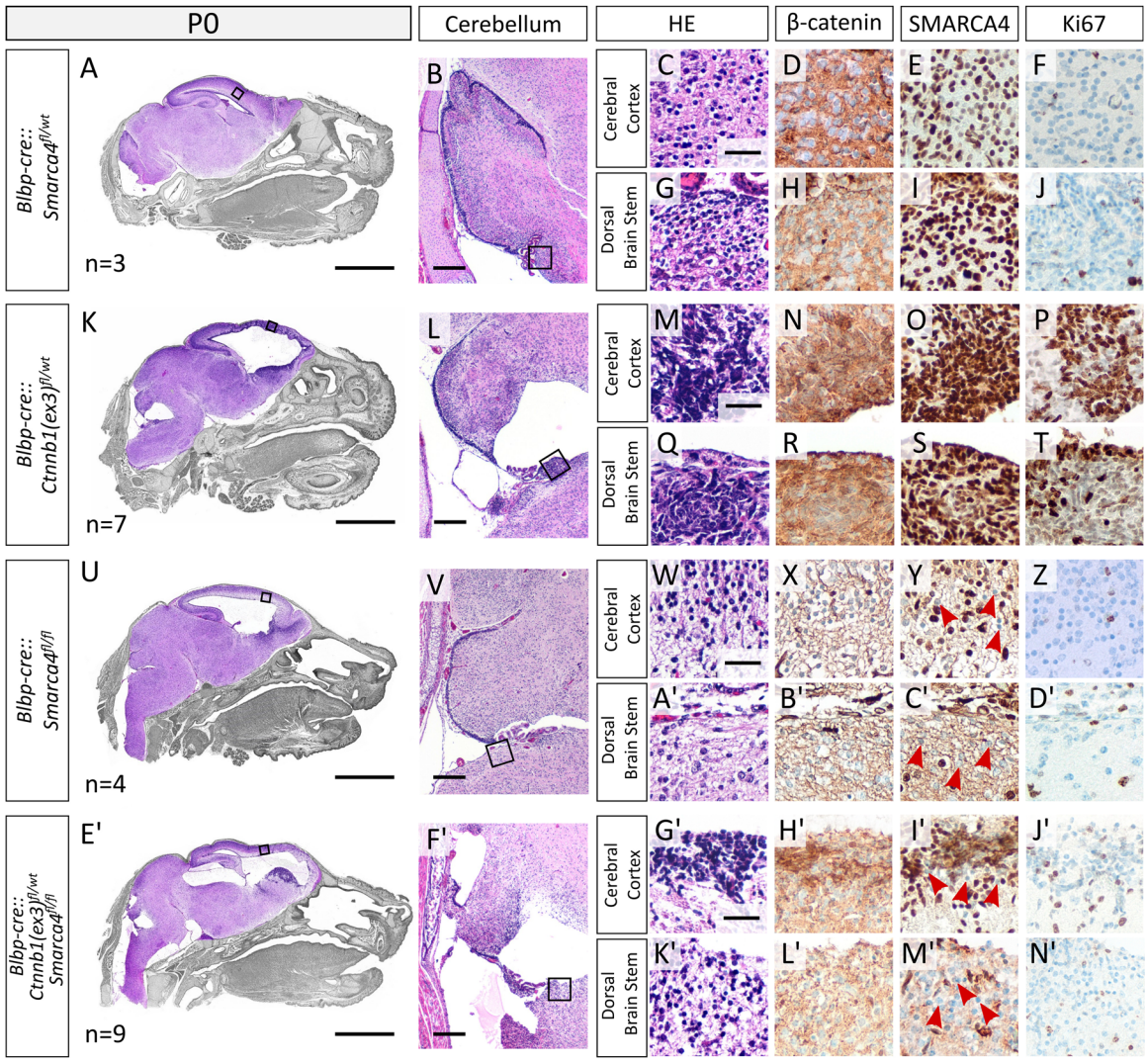

O'

Genotypes	expected	counted	counted/ exp. [%]	rel. to ctrl
Controls (cre-negative)	158.50	204	129%	100%
Blbp-cre::Smarca4$^{fl/wt}$	27.25	44	161%	125%
Blbp-cre::Smarca4$^{fl/fl}$	27.25	6	22%	17%
Blbp-cre::Ctnnb1(ex3)$^{fl/wt}$	16.75	18	107%	83%
Blbp-cre::Ctnnb1(ex3)$^{fl/wt}$ ::Smarca4$^{fl/wt}$	52.00	36	69%	54%
Blbp-cre::Ctnnb1(ex3)$^{fl/wt}$ ::Smarca4$^{fl/fl}$	35.25	9	26%	20%
Total number born		**317**	**χ^2 test: p<0.0001**	

Figure 4. Severe developmental phenotypes but no tumor development in mutants at P0. ***A***, HE staining of the sagittal section of the whole head (brain in color) of *Blbp-cre::Smarca4$^{fl/wt}$* mice at P0 reveals no phenotype. ***B***–***J***, High-power images show normally developing cerebellum, cortex, and dorsal brainstem. The cerebral cortex region is indicated by the black rectangle in ***A***, while the dorsal brainstem region is indicated by the black rectangle in ***B***. ***K***–***T***, *Blbp-cre::Ctnnb1(ex3)$^{fl/wt}$* mutants already display severe hydrocephalus, hypoplastic cerebella, and aberrant cell accumulations in both cerebral cortex and dorsal brainstem with nuclear accumulation of β-catenin at P0. *Blbp-cre::Ctnnb1(ex3)$^{fl/wt}$::Smarca4$^{fl/wt}$* mutants showed the exact same phenotype and are therefore not displayed ($n = 11$ analyzed). **U**–**D′**, *Blbp-cre::Smarca4$^{fl/fl}$* mutants also show hydrocephalus and hypoplastic cerebella but no cell accumulations in both the cortex and brainstem. Partial SMARCA4 loss is visible in both regions, with examples marked by red arrowheads (***Y***, ***C′***). ***E′***–***N′***, *Blbp-cre::Ctnnb1(ex3)$^{fl/wt}$::Smarca4$^{fl/fl}$* mutants were mostly found dead at birth and showed severe hydrocephalus and the most prominent hypoplastic cerebella. Aberrant cell accumulations in the cerebral cortex were detected in reduced quantity and size, whereas cell accumulations in the dorsal brainstem were never found. ***O′***, Counted versus expected (Mendelian ratio) genotypes detected after birth. Scale bars in ***A***, ***K***, ***U***, and ***E′*** correspond to 2 mm, in ***B***, ***L***, ***V***, and ***F***) to 200 µm, and in ***C***, ***M***, ***W***, and ***G′***) to 50 µm (applicable to all remaining panels).

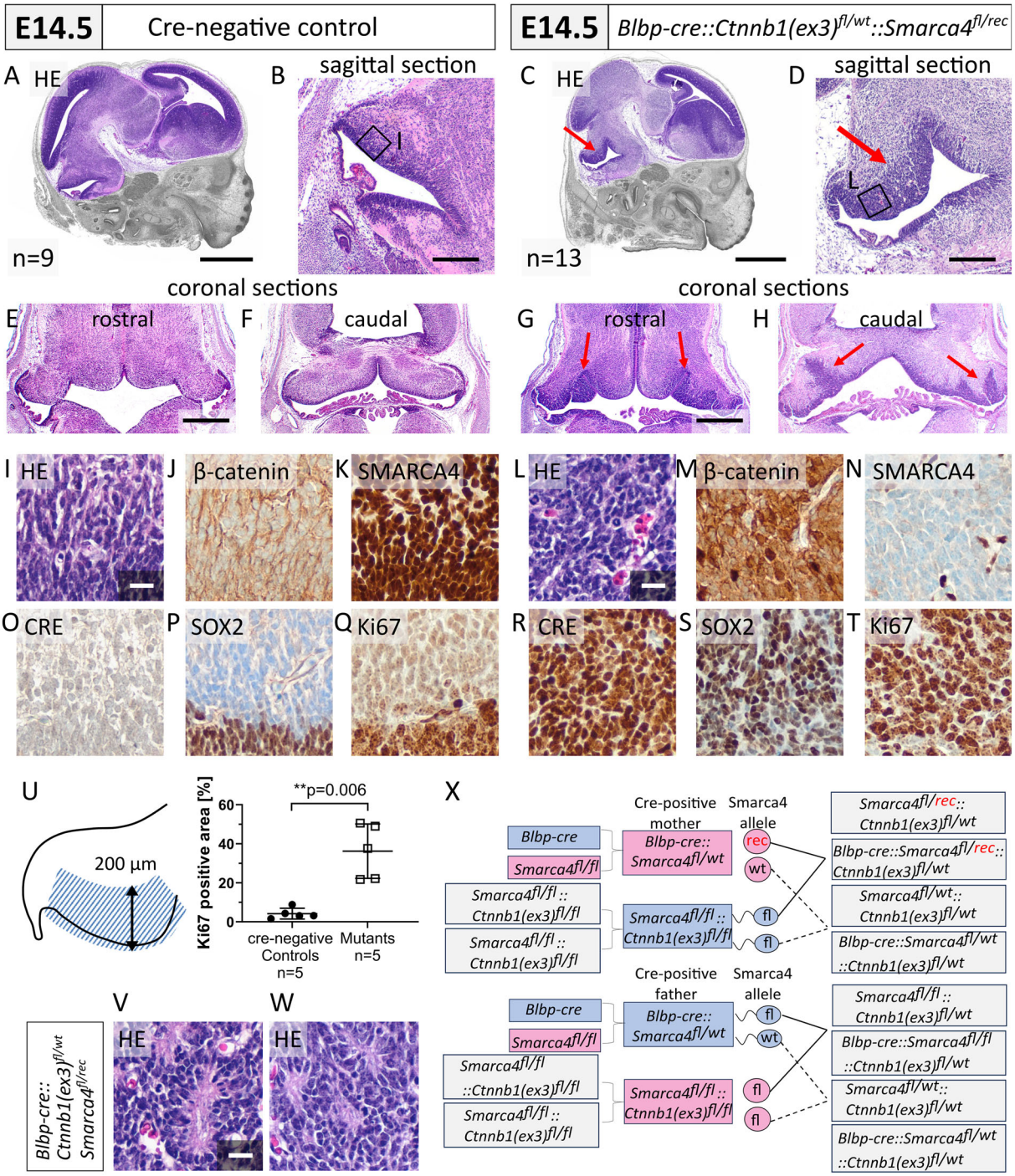

Figure 5. Combined activation of WNT signaling and loss of SMARCA4 induces proliferative lesions at embryonic age in *Blbp-cre::Ctnnb1(ex3)*$^{fl/wt}$*::Smarca4*$^{fl/rec}$ mutants. ***A–D***, HE stainings show a large lesion in the VZ of the developing cerebellum at E14.5 in *Blbp-cre::Ctnnb1(ex3)*$^{fl/wt}$*::Smarca4*$^{fl/rec}$ mutants (red arrow in ***C*** and ***D***) compared with cre-negative littermates (***A***, ***B***). ***E–H***, HE staining of coronal sections reveals the presence of lesions in the rostral as well as caudal section of the cerebellum within both hemispheres (red arrows) but excluding the midline. ***I–T***, High-power images of lesions compared with control cerebella (corresponding to black rectangles in ***B–D***) display high cell density interspersed with blood vessels (***L***), nuclear accumulation of β-catenin (***M***), loss of SMARCA4 (***N***), and positivity for cre (***R***) and SOX2 (***S***). Ki67 staining indicates high proliferation within the lesions (***T***) with a significantly increased area staining positive for Ki67 in mutants (***U***; area measured shown on the left). ***V***, ***W***, Rosette-like structures detected in HE within cerebellar lesions of mutants. ***X***, Breeding scheme of mice employed in the project illustrating the differences in breeding with cre-positive mothers passing on the recombined *Smarca4* allele (rec) and cre-positive fathers passing on the floxed *Smarca4*. A detailed description of all tissues tested for *Smarca4* recombination is provided in Extended Data Table 5-1. Scale bars in ***A***, ***C*** correspond to 1 mm, in ***B***, ***D*** to 250 µm, in ***E***, ***G*** to 500 µm (also applicable to ***F***, ***H***), and in ***I***, ***V*** to 25 µm (applicable to ***I–T***, ***W***).

single-cell RNA sequencing of cerebellar cells isolated at E16.5. In UMAP embedding, mutant cerebella displayed distinct clusters that were not present in cre-negative control cerebella (Fig. 11*A*). According to predicted cell classes as described by La Manno et al., these mutant clusters mainly resembled radial glia, neuroblasts, and neurons (Fig. 11*B*; La Manno et al., 2021). Especially radial glia were overrepresented in the mutant cerebellum with a count of 2,282 cells (16.6% of total cells)

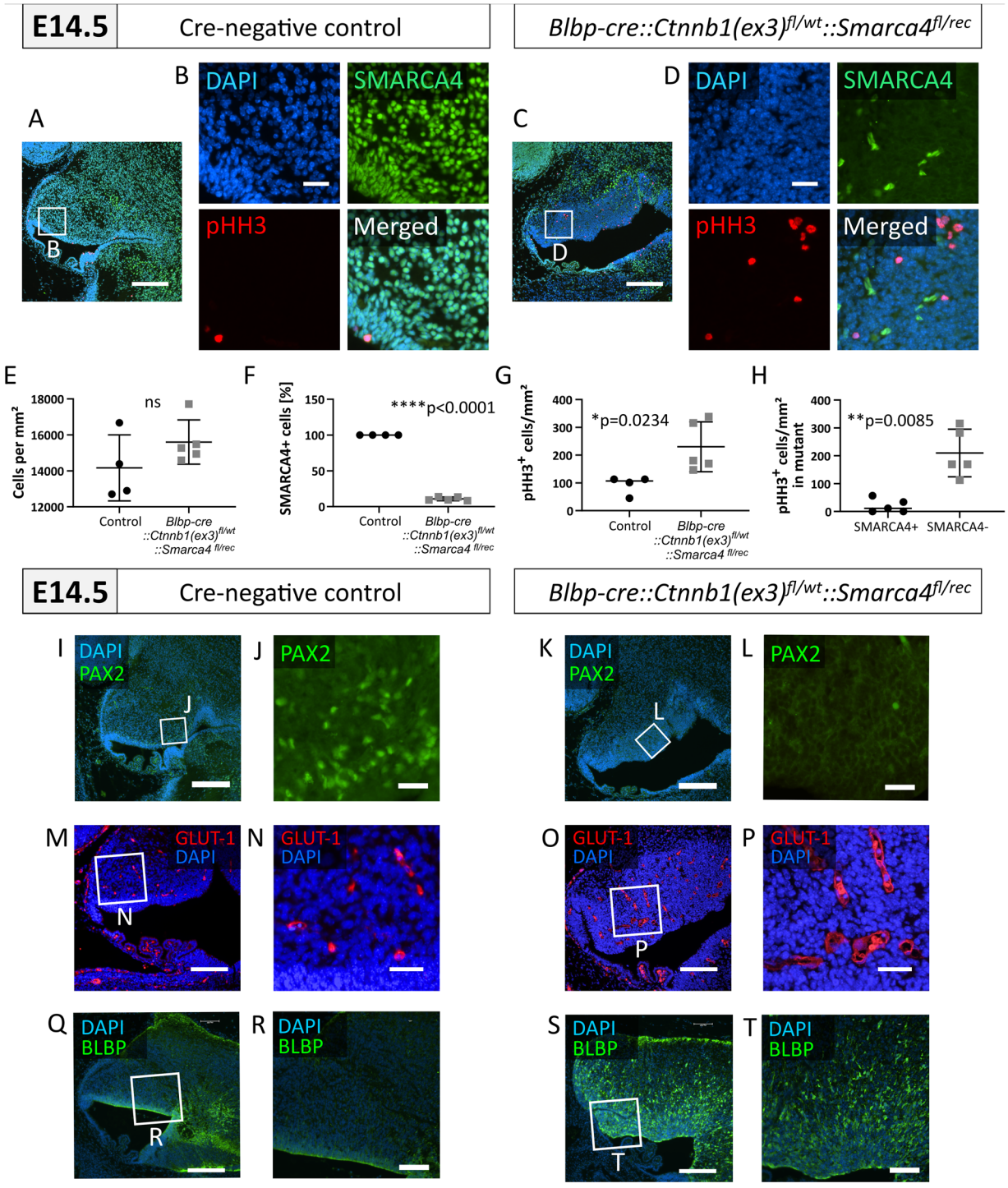

Figure 6. Cerebellar lesions in *Blbp-cre::Ctnnb1(ex3)*$^{fl/wt}$*::Smarca4*$^{fl/rec}$ mutants show increased mitotic count, loss of interneuron progenitor populations, and an intact blood–brain barrier. ***A–D***, IF costaining of SMARCA4 and pHH3 in the VZ of controls and mutants (*Blbp-cre::Ctnnb1(ex3)*$^{fl/wt}$*::Smarca4*$^{fl/rec}$) at E14.5 (controls $n = 4$, mutants $n = 5$). ***E***, Cell density according to DAPI signal in SMARCA4/pHH3 costaining. ***F***, SMARCA4-positive cells according to SMARCA4/pHH3 costaining. ***G***, Mitotic cell count according to SMARCA4/pHH3 costaining. ***H***, Mitotic cell count with or without concurrent SMARCA4 signal within mutant samples. ***I***, ***J***, PAX2 staining shows the migration of interneuron progenitors from the VZ inwards in control animals. ***K***, ***L***, PAX2-positive interneuron progenitors are not detected in the VZ of mutant animals. ***M–P***, Blood vessels in controls as well as mutants show positivity for GLUT-1, suggesting a maintained blood–brain barrier within the lesion. ***Q–T,*** The cells in the VZ in controls and in the lesions in the mutants express BLBP. Scale bars in ***A***, ***C*** correspond to 200 µm, in ***B***, ***D*** to 25 µm; in ***I***, ***K*** to 200 µm; in ***J***, ***L*** to 25 µm; in ***M***, ***O***, ***Q***, and ***S*** to 100 µm; in ***N***, ***P*** to 25 µm; and in ***R*** and ***T*** to 50 µm.

compared with 886 cells (6.4% of total cells) in the control cerebellum (Extended Data Table 11-1*A*,*B*). A more detailed prediction of cell subclasses according to La Manno et al. predominantly assigned cells within mutant clusters to "hindbrain," "hindbrain glycinergic," "hindbrain glutamatergic," "Bergmann glia," or "undefined" populations (Extended Data Table 11-1*C*,*D*). Overall, the number of glutamatergic cerebellar cells in mutants was highly reduced compared with controls [3,090 in control (22.5% of total cells) vs 1,062 in mutant (7.74% of total cells); Extended Data Table 11-1*C*,*D*].

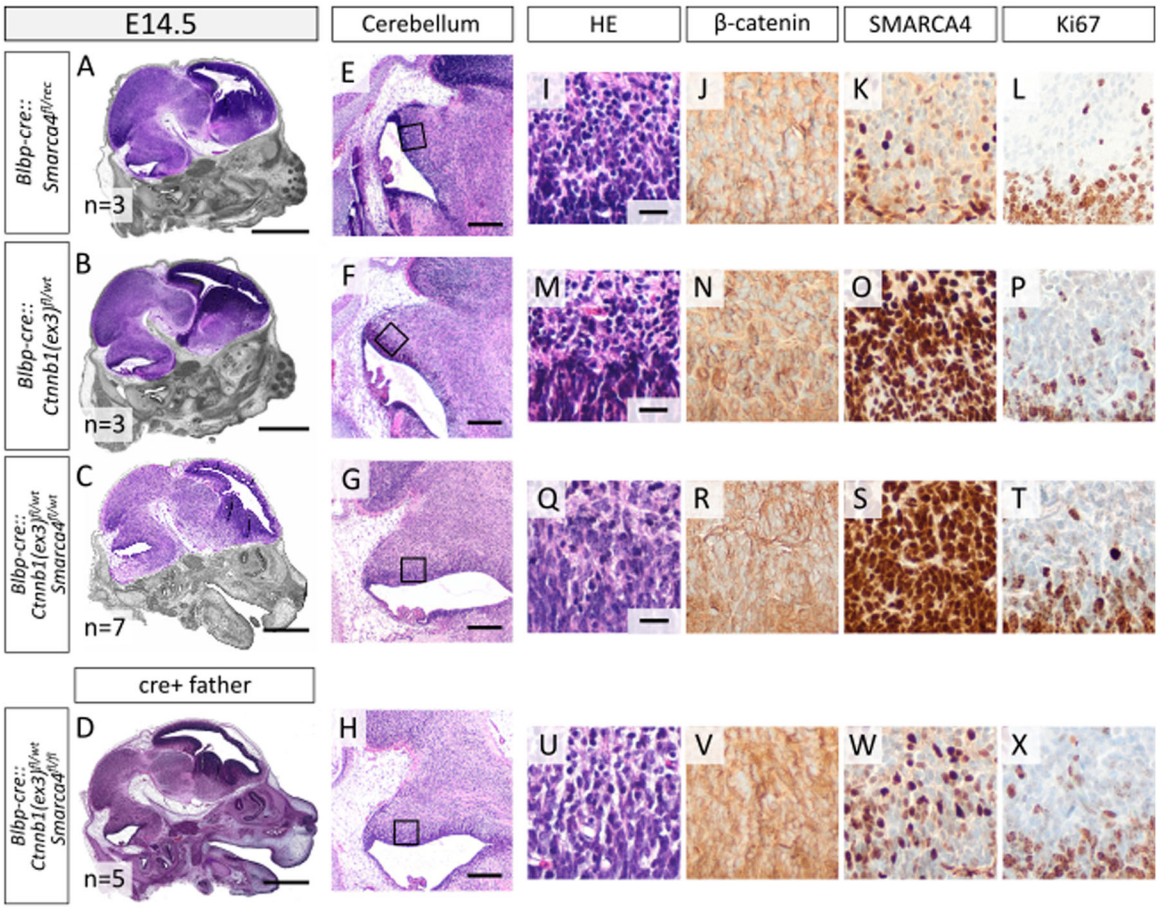

Figure 7. Cerebellar lesions are not detected in other mutant genotypes at E14.5. ***A–D***, HE stainings of whole head sagittal sections of *Blbp-cre::Smarca4*$^{fl/rec}$, *Blbp-cre::Ctnnb1(ex3)*$^{fl/wt}$, and *Blbp-cre::Ctnnb1(ex3)*$^{fl/wt}$*::Smarca4*$^{fl/wt}$ mutants derived from cre-positive mothers and *Blbp-cre::Ctnnb1(ex3)*$^{fl/wt}$*::Smarca4*$^{fl/fl}$ mutants derived from cre-positive fathers at E14.5. ***E–H***, Higher magnification of cerebellar areas in sagittal HE stainings. ***I–X***, HE and DAB stainings of the VZ, areas correspond to black rectangles in ***E–H***. ***J–W***, Nuclear accumulation of β-catenin is not evident in any of the genotypes, whereas partial loss of SMARCA4 is visible in *Blbp-cre::Smarca4*$^{fl/rec}$ and *Blbp-cre::Ctnnb1(ex3)*$^{fl/wt}$*::Smarca4*$^{fl/fl}$ mice only. ***L–X***, Proliferation in the VZ is not increased in mutants according to Ki67 stainings. Scale bars in ***A–D*** correspond to 1 mm, in ***E–H*** to 200 µm, and in ***I***, ***M***, and ***Q*** to 20 µm (also applicable to ***J–X***).

Next, we predicted the age of cells according to the same reference dataset, including only data from E10.0 to E16.5 (La Manno et al., 2021). While most cells within the control clusters were assigned to E15.0-E16.5, mutant clusters also included a considerable number of cells with predicted ages between E11.0 and E14.0, hinting toward a rather undifferentiated nature of mutant cells (Fig. 11*C*). Cluster 6 displayed the highest deviation from expected age with a mean predicted age of 14.38 embryonic days (Extended Data Table 11-2).

Cell cycle analysis identified both Clusters 2 and 9 as mitotically active, with all cells assigned to the G2M or S phase (Fig. 11*D*). While Cluster 2 mainly consists of cells derived from the control cerebellum, Cluster 9 is a mutant cluster that could represent a potentially tumorigenic aberrant cell population within the lesions. Increased expression of SOX2, which stained positive in previous histological analyses of cerebellar lesions, was evident in mutant Clusters 9 and 17 and to a smaller extent in Cluster 0 (Fig. 11*E*). Additionally, all three clusters displayed high levels of *Dkk3*, *Wnt5a*, *Dkk2*, *Lef1*, *Axin2*, *Dkk1*, and *Wif1*, which have all been associated with activated WNT signaling before (Gibson et al., 2010; Zhang et al., 2011; Latour et al., 2021). The top significantly higher expressed genes within Clusters 0, 6, 8, 9, 17, and 19 compared with remaining clusters included WNT targets *Wif1* and *Nkd1*, which both act as negative regulators of WNT signaling and also show increased expression in WNT MB (Gibson et al., 2010; Phoenix et al., 2016; Luo et al., 2021; Fig. 11*F*, Extended Data Table 11-3*A*). Moreover, genes associated with the extracellular matrix and actin cytoskeleton (e.g., *Tmem132c* and *Lingo2*) were overexpressed in mutants (Sanchez-Pulido and Ponting, 2018; Jo et al., 2019). Other highly expressed genes in mutant clusters play an important role in neurogenesis and synaptic transmission (*Rbfox1*, *Tenm2*, and *Rgs6*; Ahlers et al., 2016; Vuong et al., 2018; Zhang et al., 2022). In contrast, mutant clusters displayed lower expression of genes associated with the differentiation of glutamatergic cerebellar neurons (*Neurod1*, *Pax6*, and *Gm2694*; Engelkamp et al., 1999; Pan et al., 2009; Jin et al., 2021). GSEA further validated the upregulation of WNT signaling in mutant clusters (Extended Data Table 11-3*B*).

To gain insights into the origin of aberrant mutant clusters and their developmental trajectory, we performed trajectory analysis using only cells from mutant Clusters 0, 6, 8, 9, 17, and 19. According to pseudotime, cells of mutant Cluster 9 were rather assigned to the beginning of the trajectory, while Cluster 0 was distributed across all stages and Cluster 6 represented the major population at the end of the trajectory (Fig. 12*A*,*B*). RNA velocity analysis resulted in similar patterns, with cells originating from Cluster 9 and transitioning to Cluster 6 via Cluster 0 (Fig. 12*C*,*D*). Gene expression patterns

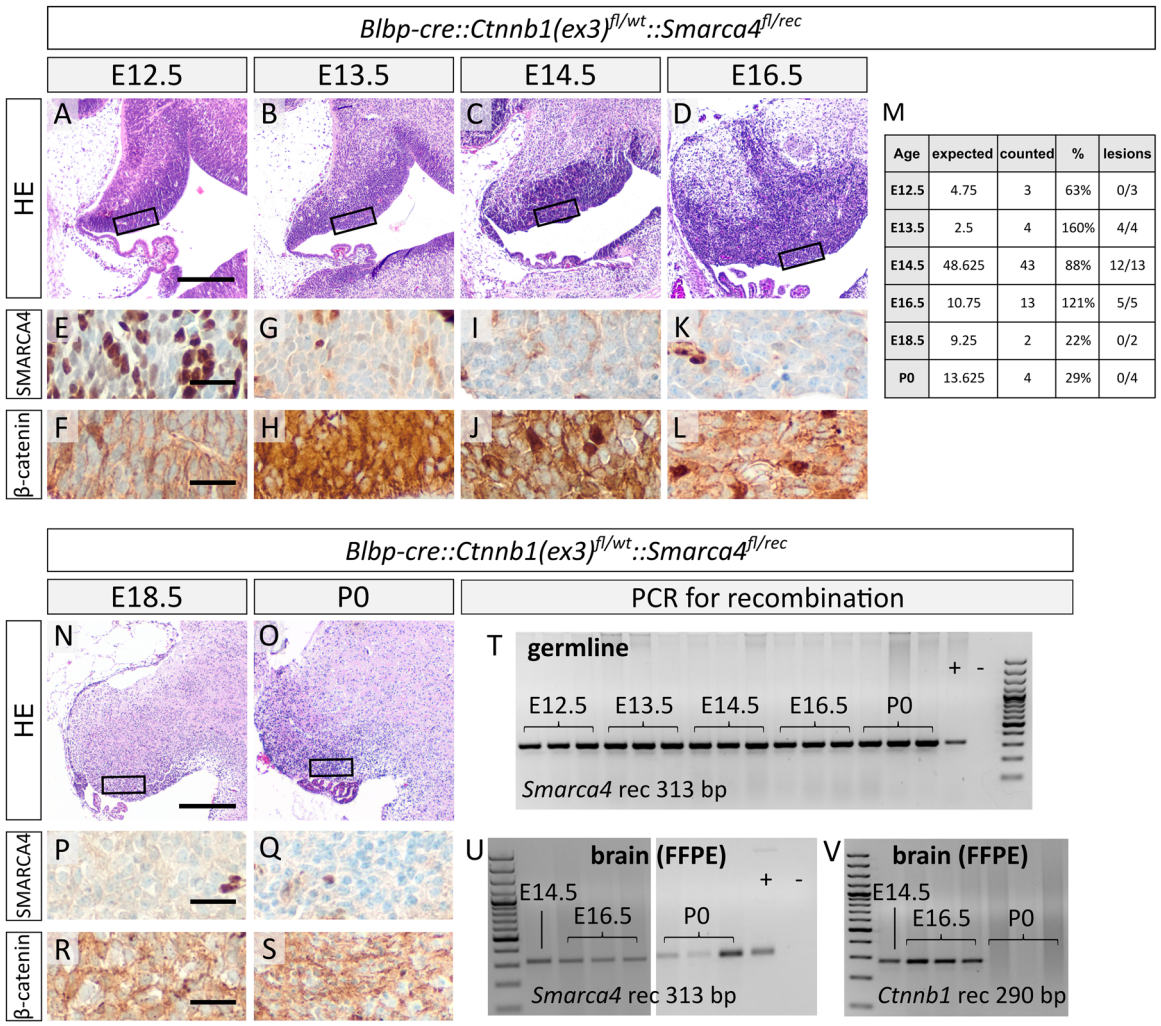

Figure 8. Cerebellar lesions develop from E13.5 to E16.5. ***A–D***, HE stainings of *Blbp-cre::Ctnnb1(ex3)*$^{fl/wt}$*::Smarca4*$^{fl/rec}$ brains show cerebellar development from E12.5 to E16.5 with lesions visible from E13.5 to E16.5. ***E–L***, SMARCA4 and β-catenin stainings of the cerebellar VZ (black rectangle in ***A–D***) reveal a partial loss of SMARCA4 at E12.5 and complete SMARCA4 loss from E13.5. Nuclear accumulation of β-catenin is visible in lesions from E13.5 to E16.5. ***M***, Expected versus counted genotypes in litters of cre-positive mothers at different embryonic stages and P0. Column "%" = percentage counted/expected; column "lesions" = count of cerebellar lesions in histologically analyzed mutants. ***N–O***, *Blbp-cre::Ctnnb1(ex3)*$^{fl/wt}$*::Smarca4*$^{fl/rec}$ cerebella without any evidence of lesions. ***P–S***, SMARCA4 and β-catenin stainings of the cerebellar VZ (corresponding to the black rectangle in ***N*** and ***O***). ***T***, Recombination of *Smarca4* tested by PCR in genomic DNA from tail biopsies of histologically analyzed mutants from E12.5 to P0 shows recombination at all ages tested. ***U***, *Smarca4* recombination was also detected using DNA isolated from FFPE sections of mutant brains. ***V***, Using the same DNA samples as in ***U***, recombination of *Ctnnb1* was only detected at E14.5 and E16.5 but not in mutants analyzed at P0. Scale bars in ***A*** and ***N*** correspond to 250 µm (also applicable to ***B–D*** and ***O***) and in ***E***, ***F***, ***P***, and ***R*** to 25 µm (also applicable to ***G–L*** and ***Q–S***).

along this transition first showed increasing expression of WNT targets (*Lef1*, *Wif1*, *Nkd1*) followed by high expression of genes associated with neuronal differentiation (e.g., *Tubb3* and *Map1b*) in Cluster 6 (Meixner et al., 2000; Tischfield et al., 2010; Fig. 12*D*).

Analysis of in vitro proliferation and tumorigenic potential of cerebellar lesions

To evaluate the tumorigenic potential of cerebellar lesions detected in *Blbp-cre::Ctnnb1(ex3)*$^{fl/wt}$*::Smarca4*$^{fl/rec}$ mutants, HPCs were isolated from controls and mutants at E14.5. Cumulative PD during cell culture as neurospheres for four weeks did not show any significant differences between the proliferation of cre-negative controls, mutants (*Blbp-cre::Ctnnb1(ex3)*$^{fl/wt}$*::Smarca4*$^{fl/rec}$), and heterozygous mutants (*Blbp-cre::Ctnnb1(ex3)*$^{fl/wt}$*::Smarca4*$^{fl/wt}$; Fig. 13*A*). Morphologically, neurospheres of mutants did not differ from controls (Fig. 13*B*,*C*). Moreover, mutants maintained dependency on EGF and FGF in adherent cell cultures on PLO-coated wells (Fig. 13*D–G*). IF stainings at early time points in culture (Passage 0) showed a loss of SMARCA4 in the majority of cells derived from mutants (Fig. 13*H*). However, the percentage of SMARCA4-positive cells significantly increased until Passage 1, suggesting a selection for SMARCA4-positive cells in vitro over time ($t = 5.223$, DF = 3.898, $p = 0.0069$, Welch's t test; Fig. 13*I*,*J*). According to IF costaining of SMARCA4 and BrdU, SMARCA4-positive cells already showed significantly higher proliferation at Passage 0 in mutants ($t = 3.297$, DF = 3, $p = 0.0458$, paired t test; Fig. 13*K*). Additionally, an evaluation of recombined β-catenin in DNA isolated at different passages of mutant HPCs showed a loss of the recombined allele from Passage 2 (Fig. 13*L*). Altogether, data pointed toward a loss of recombined cells after HPC culture from mutant cerebella in vitro. We hypothesized that the in vitro environment did not

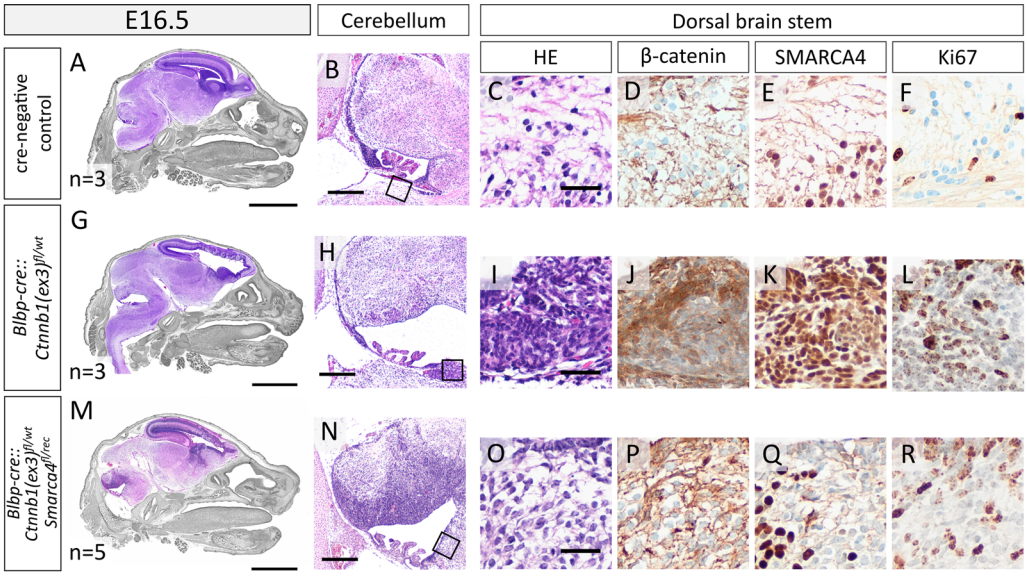

Figure 9. *Blbp-cre::Ctnnb1(ex3)$^{fl/wt}$::Smarca4$^{fl/rec}$* mutants do not develop brainstem lesions. ***A–F***, HE stainings of cre-negative controls at E16.5 show normally developing cerebellum with low cell density in HE (***B***, ***C***), absence of β-catenin accumulation (***D***), positivity for SMARCA4 (***E***), and low proliferation (***F***). Meanwhile, *Blbp-cre::Ctnnb1(ex3)$^{fl/wt}$* mice display aberrant cell accumulations in the dorsal brainstem with high cell density (***G***, ***H***), nuclear accumulation of β-catenin (***J***), and SMARCA4-positive cells with increased proliferation (***K***, ***L***). *Blbp-cre::Ctnnb1(ex3)$^{fl/wt}$::Smarca4$^{fl/rec}$* mutants display the beforementioned cerebellar lesions (***M***, ***N***) but do not develop any cell accumulations in the brainstem (***O***, ***P***). Loss of SMARCA4 is apparent in the affected region (***Q***). Scale bars in ***A***, ***G***, and ***M*** correspond to 2 mm; in ***B***, ***H***, and ***N*** to 250 µm; and in ***C***, ***I***, and ***O*** to 20 µm (also applicable to the remaining panels). Only the offspring of cre-positive mothers were included in the analysis.

provide the required scaffold and paracrine signals from surrounding cells needed for survival and extensive proliferation of recombinant cells. Therefore, we transplanted E14.5 HPCs of controls, mutants, and heterozygous mutants ($n = 10$ each) into the cerebella of adult immunodeficient mice to evaluate tumorigenic potential in vivo. To avoid negative selection of recombined cells, we performed transplantation directly after papain digestion and singularization of hindbrain tissue (Fig. 13*M*). However, no tumor development was detected in any of the groups 6 months after transplantation. To further evaluate the impact of an embryonic microenvironment on cell proliferation, we cultured cerebellar explants of E14.5 mutant cerebella on coated dishes without dissociation into single cells. In this setting, SMARCA4-deficient cells efficiently migrated from the explants and showed significantly increased proliferation compared with SMARCA4-positive cells ($t = 3.697$, DF = 9, $p = 0.0049$, paired t test; Fig. 13*N*,*O*). Altogether, these observations suggest an important role of the embryonic microenvironment in the development of lesions and maintenance of high proliferation.

Discussion

In this work, we generated *Blbp-cre::Ctnnb1(ex3)$^{fl/wt}$::Smarca4$^{fl/rec}$* mice that were not viable after birth but presented highly proliferative lesions in the embryonic cerebellum. Lesions did not occur upon alteration of *Ctnnb1* or *Smarca4* alone, which provides proof for a cooperative interaction between aberrant WNT signaling and a loss of SMARCA4. An in-depth analysis of lesions by histology, DNA methylation profiling, and single-cell RNA sequencing revealed their probable cellular origin and potentially involved deregulated pathways. Furthermore, in vitro experiments showed a negative selection of recombined cells and suggested an important role of the embryonic microenvironment in the development of lesions.

Our first observation was the severe phenotype of *Blbp-cre::Ctnnb1(ex3)$^{fl/wt}$* mice with short survival, severe hydrocephalus, and hypoplastic cerebella that was not described before (Gibson et al., 2010). Fate mapping confirmed much broader recombination driven by our *Blbp-cre* line than previously published, which could easily explain the discrepancy between phenotypes (Gibson et al., 2010). In fact, our model displayed phenotypes similar to previously described *hGFAP-cre::Ctnnb1(ex3)$^{fl/wt}$* mice with hydrocephalus, hypoplastic cerebella, and underdeveloped cerebral cortices (Pöschl et al., 2013). Consequently, it is quite probable that our *Blbp-cre* line encompasses a broad overlap with cell populations targeted by *hGFAP-cre* in the brain. This is further supported by phenotypes of our *Blbp-cre::Smarca4$^{fl/fl}$* mutants at P0, which resemble previously described *hGFAP-cre::Smarca4$^{fl/fl}$* mice (Holdhof et al., 2020). A mix-up of mouse lines per accident was ruled out by the detection of lacZ in the PCR analysis of our *Blbp-cre* mice (data not shown). Furthermore, our *Blbp-cre::Ctnnb1(ex3)$^{fl/wt}$* mutants did not develop other characteristics specific to *hGFAP-cre::Ctnnb1(ex3)$^{fl/wt}$* mice such as no development of fur, missing ability to open their eyes or missing hippocampal structures (Pöschl et al., 2013). Hydrocephalus is also known to occur spontaneously in *C57Bl6/J* mice and can be enriched by inbreeding (Vogel et al., 2012). Therefore, we evaluated the influence of the genetic background by performing backcrossings of our *Ctnnb1(ex3)$^{fl/fl}$* and *Blbp-cre* lines to both *C57Bl6/J* and *129S2/Sv* mice for at least five generations. However, both variations did not result in any alteration of the phenotype in *Blbp-cre::Ctnnb1(ex3)$^{fl/wt}$* offspring (data not shown). Consequently, we hypothesize that the difference in cre expression is a result of genetic drift between our *Blbp-cre* line and previously used colonies, a common phenomenon for inbred mouse strains (Stevens et al., 2007; Benavides et al., 2020).

Cell accumulations in the brainstem lesions of our *Blbp-cre::Ctnnb1(ex3)$^{fl/wt}$* mice were similar to those described before

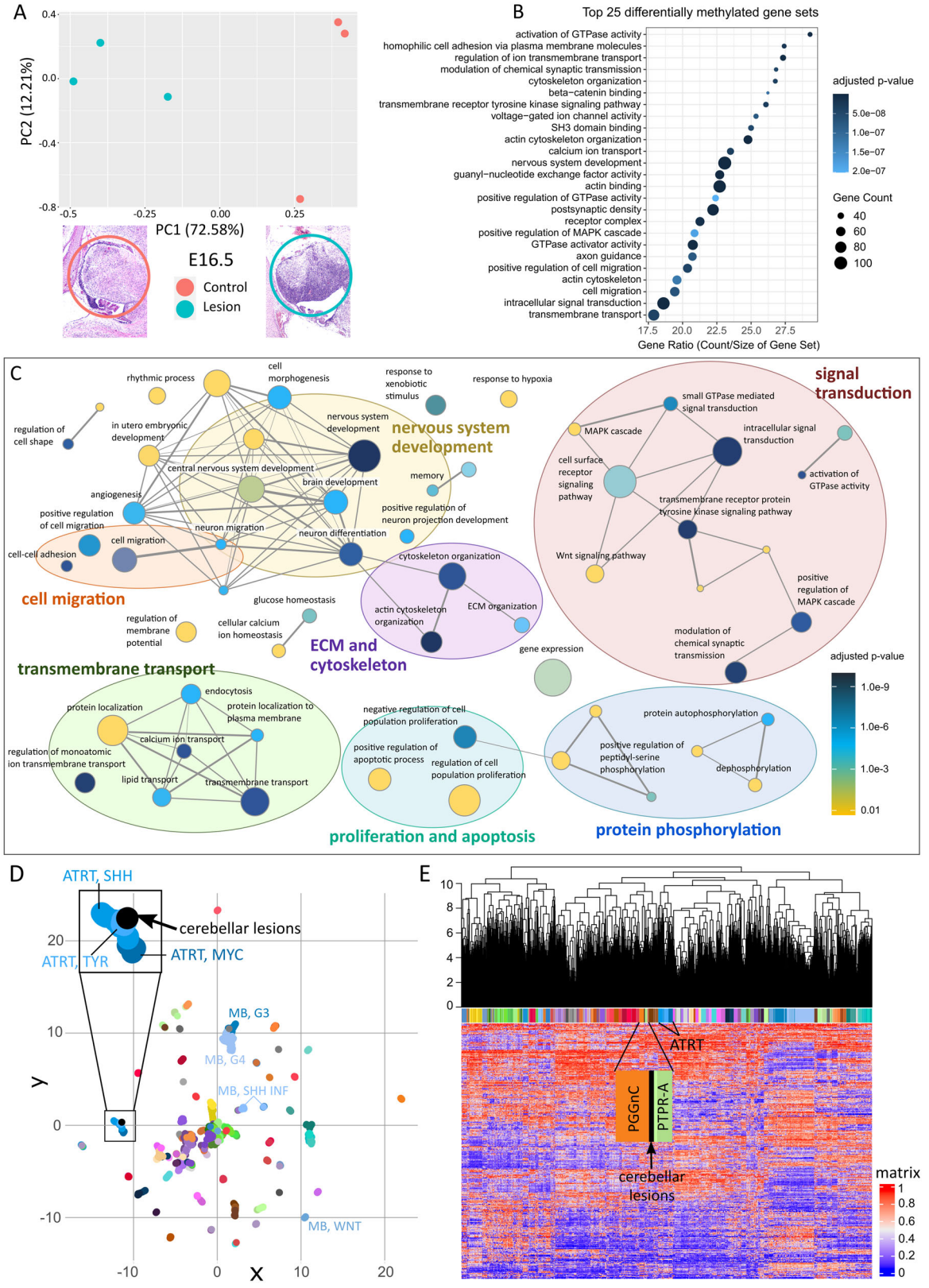

Figure 10. Continued.

and can be attributed to stalled migration of mossy fiber neuron precursors (Gibson et al., 2010). The additional non-proliferative cell accumulations in the cerebellum of our mice might similarly consist of neural progenitors unable to differentiate and migrate to their final position in the cerebellum. This is further supported by their expression of SOX2 and nestin and the absence of markers associated with more differentiated cell types. The fact that *Blbp-cre::Ctnnb1(ex3)$^{fl/wt}$::Smarca4$^{fl/rec}$* mice did not develop any cell accumulations in the brainstem suggests that SMARCA4 loss prevents stalled migration of mossy fiber neuron precursors. Since SMARCA4 plays an important role in neurogenesis, a loss of SMARCA4 might hamper early differentiation toward this lineage, consequently also blocking their accumulation (Matsumoto et al., 2006; Holdhof et al., 2020).

In contrast to cell accumulations in the postnatal cerebellum, embryonic cerebellar lesions in *Blbp-cre::Ctnnb1(ex3)$^{fl/wt}$::Smarca4$^{fl/rec}$* mutants were highly proliferative and vastly expanded from E13.5 to E16.5. Lesions were localized in the VZ, stained positive for SOX2, and prevented the formation and migration of PAX2-positive interneuron progenitors. This observation suggests an origin in GABAergic progenitors, which reside in the VZ in embryonic brain development and give rise to Purkinje cells and inhibitory interneurons (Martinez et al., 2013; van Essen et al., 2020). However, Zhang et al. have recently described a SOX2-positive progenitor cell population that can give rise to all known cerebellar precursors of both URL and VZ and could be affected by *Blbp*-targeted recombination (Hegedus et al., 2007; Zhang et al., 2021).

The count of *Blbp-cre::Ctnnb1(ex3)$^{fl/wt}$::Smarca4$^{fl/rec}$* mutants was as expected from E12.5 until E16.5 but highly reduced at E18.5 and P0, suggesting prenatal lethality induced by the expanding lesions. Moreover, the few mutants found at E18.5 and P0 did not develop cerebellar lesions, which we attributed to the missing recombination of *Ctnnb1* as detected by PCR. Different degrees of recombination between animals of the same genotype have been described before, for example, in *GFAP-cre*–driven models (Requardt et al., 2009; Pöschl et al., 2013). Moreover, floxed alleles have differential sensitivities to cre-mediated recombination, which could explain a more efficient recombination of *Smarca4* than *Ctnnb1* in our mice (Liu et al., 2013; Luo et al., 2020). In addition to this phenomenon, we detected germline recombination of *Smarca4* in all offspring of cre-positive mothers, which highly influenced observed phenotypes. A recent evaluation of recombination in CNS-specific cre-driver lines revealed unexpected germline recombination as a very common phenomenon, affecting more than half of all commonly used lines (Luo et al., 2020). In our model, germline recombination of one *Smarca4* allele was essential for the development of cerebellar lesions in mutants. These observations stress the necessity to test for germline recombination in every new cre-driven mouse model.

The fact that lesions were not located in the brainstem but in the cerebellum and stained positive for GLUT-1 indicating a functional blood–brain barrier argues against similarity to early tumorous lesions in the WNT MB model *Blbp-cre::Ctnnb1(ex3)$^{fl/wt}$::Trp53$^{fl/fl}$* (Gibson et al., 2010). This was also reflected by our comparison of global DNA methylation of cerebellar lesions to human brain tumors, which did not yield a reliable match. Hence, our model probably does not recapitulate the biological origin of WNT MB in the mossy fiber neuron lineage. However, the transformation of cells in the cerebellar VZ raises the question if other cell populations might be prone to tumor development upon deregulated WNT signaling and chromatin remodeling. Moreover, our *Blbp-cre::Ctnnb1(ex3)$^{fl/wt}$::Smarca4$^{fl/rec}$* model is the first one to show a cooperative effect between mutated β-catenin and loss of SMARCA4 in promoting extensive proliferation. Others have hypothesized before that the development of WNT MB requires disruption of chromatin remodeling at WNT-responsive genes in addition to the stabilization of β-catenin (Robinson et al., 2012). This is reflected by the finding that WNT MB not only show a high frequency of *SMARCA4* mutations but also of other chromatin modifiers such as acetyltransferase *CREBBP*, BAF complex subunits *ARID1A/ARID2*, or methyl transferase *KMT2D* (Robinson et al., 2012; Northcott et al., 2017; Gajjar et al., 2021). Nuclear β-catenin can directly interact with both SMARCA4 and CBP proteins to regulate transcription of WNT-responsive genes (Mosimann et al., 2009; Sharma et al., 2023). Changing or eliminating this interaction might be essential for the transformation of cells since both *Ctnnb1* and *Smarca4* alterations on their own did not suffice to form lesions.

Molecular analysis of cerebellar lesions revealed aberrant WNT signaling and deregulated organization of the actin cytoskeleton on both DNA methylation levels and in single-cell RNA sequencing. Remodeling of the actin and tubulin cytoskeleton is essential for brain tumor cell migration and invasion and emphasizes the potentially tumorigenic nature of cerebellar lesions (Hall, 2009; Nürnberg et al., 2011). Furthermore, mutant clusters identified in single-cell RNA sequencing revealed characteristics of radial glia cells with a resemblance to early embryonic ages, which supports their previously suspected origin in early progenitor cells. The fact that the majority of glutamatergic cerebellar cells were missing in mutants compared with controls suggests that progenitors of the glutamatergic lineage were affected by recombination, again reinforcing the theory about an origin in SOX2-positive bipotent cerebellar progenitors (Zhang et al., 2021). Additionally, we identified high mitotic activity specifically in mutant Cluster 9, which could represent the cellular origin of cerebellar lesions according to trajectory and RNA velocity analysis.

In vitro, HPCs of *Blbp-cre::Ctnnb1(ex3)$^{fl/wt}$::Smarca4$^{fl/rec}$* mutants did not show increased proliferation and were prone

←

Figure 10. DNA methylation analysis of cerebellar lesions at E16.5. ***A***, E16.5 control cerebella and lesions of *Blbp-cre::Ctnnb1(ex3)$^{fl/wt}$::Smarca4$^{fl/rec}$* mutants can be clearly separated according to 10,000 most differentially methylated CpG sites in PCA analysis. Recombined alleles of *Smarca4* and *Ctnnb1* in the cerebellar DNA of mutants were confirmed by PCR. ***B***, Top 25 differentially methylated gene sets between controls and lesions according to adjusted *p*-value (*methylRRA* was applied; Ren and Kuan, 2019) sorted by gene ratio (count/size of gene sets). ***C***, All significantly differentially methylated gene sets of the category "biological process" found with *methylRRA* were summarized by REVIGO to remove redundant terms (Supek et al., 2011). Here, 3% of the strongest GO terms pairwise similarities are designated as edges in the graph. The size of bubbles corresponds to the size of gene sets. ***D***, UMAP embedding according to DNA methylation of cerebellar lesions of *Blbp-cre::Ctnnb1(ex3)$^{fl/wt}$::Smarca4$^{fl/rec}$* mice at E16.5 (Mouse Methylation BeadChip, Illumina) and human brain tumors (Capper et al., 2018; Sharma et al., 2019; in-house analyzed samples, total $n = 1,683$) using 491 orthologous CpG sites out of the 15,000 most differentially methylated CpG sites within the human dataset. Mouse samples show the most similarity to ATRT subgroups. ***E***, Heatmap clustering according to DNA methylation of the same samples and CpG sites shows the proximity of cerebellar lesions to PGGnC [paraganglional, spinal non-CIMP (CpG island methylator phenotype)] and PTPR-A (papillary tumor of the pineal region, group ***A***). MB, G3 = Group 3 MB; MB, G4 = Group 4 MB; MB SHH INF = infant SHH MB; ATRT, TYR = ATRT of the tyrosine kinase subgroup; ATRT, MYC = ATRT of the MYC subgroup; ATRT, SHH = ATRT of the SHH subgroup.

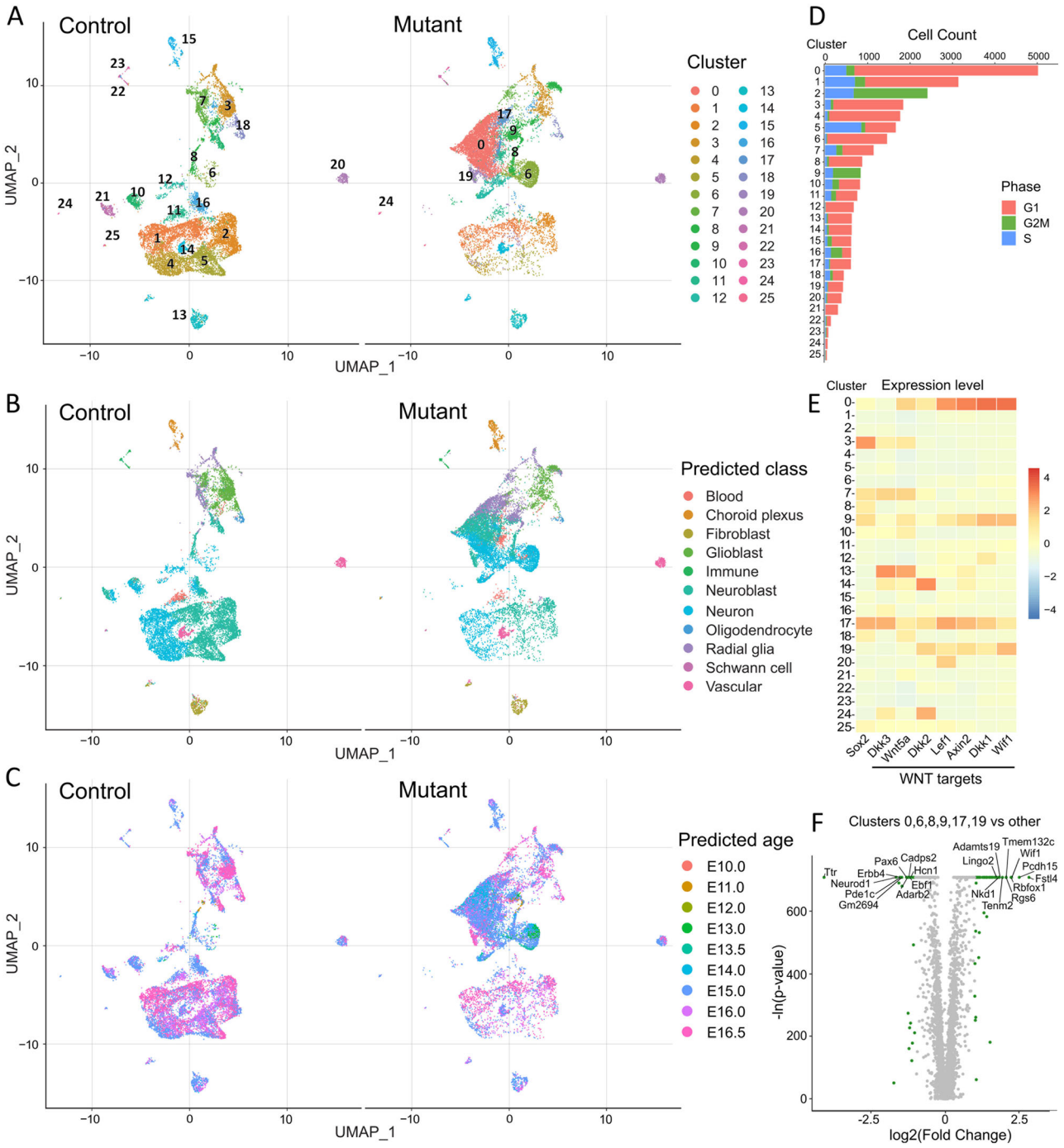

Figure 11. Single-cell RNA sequencing analysis at E16.5 reveals distinct mutant clusters of undifferentiated nature. ***A***, UMAP embedding of clusters derived from single cells of control and mutant (*Blbp-cre::Ctnnb1(ex3)*$^{fl/wt}$*::Smarca4*$^{fl/rec}$) cerebella at E16.5. In total, 25 clusters were identified, of which Clusters 0, 6, 8, 9, 17, 19, and 24 mainly consist of mutant cells. ***B***, Cell classes were predicted according to a murine reference dataset (La Manno et al., 2021), showing an increased number of radial glia cells in mutant clusters. Cell counts of each class are listed in Extended Data Table 11-1*A* and *B*. A more detailed prediction of cell subclasses is shown in Extended Data Table 11-1*C* and *D*. ***C***, Age predictions according to the La Manno et al. (2021) reference dataset from E10.0 to E16.5 suggest a more undifferentiated nature of cells within mutant clusters. Respective cell counts for predicted ages are listed in Extended Data Table 11-2. ***D***, Cell cycle analysis identified high mitotic activity in both Cluster 2 and mutant Cluster 9 with all cells assigned to the G2M and S phase. ***E***, The expression level of *Sox2* and WNT target genes is increased in mutant clusters, especially affecting Clusters 0, 9, and 17. ***F***, DEGs in Clusters 0, 6, 8, 9, 17, and 19 compared with other clusters (labeled green with cut off at log2 fold change ≥ 1 and adjusted $p < 0.01$, Wilcoxon rank sum test, Bonferroni's correction). A list of DEGs and enriched gene sets in mutant clusters is provided in Extended Data Table 11-3.

to selection for non-recombined cells over time. We have shown before that SMARCA4-deficient neurospheres have a selection disadvantage in vitro (Holdhof et al., 2021a). However, even direct transplantation of mutant HPCs into adult immunodeficient mice did not induce brain tumor formation, which argues against their tumorigenic potential. Nevertheless, the tumorigenic potential of *Ctnnb1* and *Smarca4* altered cells might depend on an embryonic microenvironment that cannot be provided by adult brain tissue of immunodeficient mice. This was supported by cerebellar explant cultures without dissociation into single cells, which resulted in increased proliferation of SMARCA4-deficient

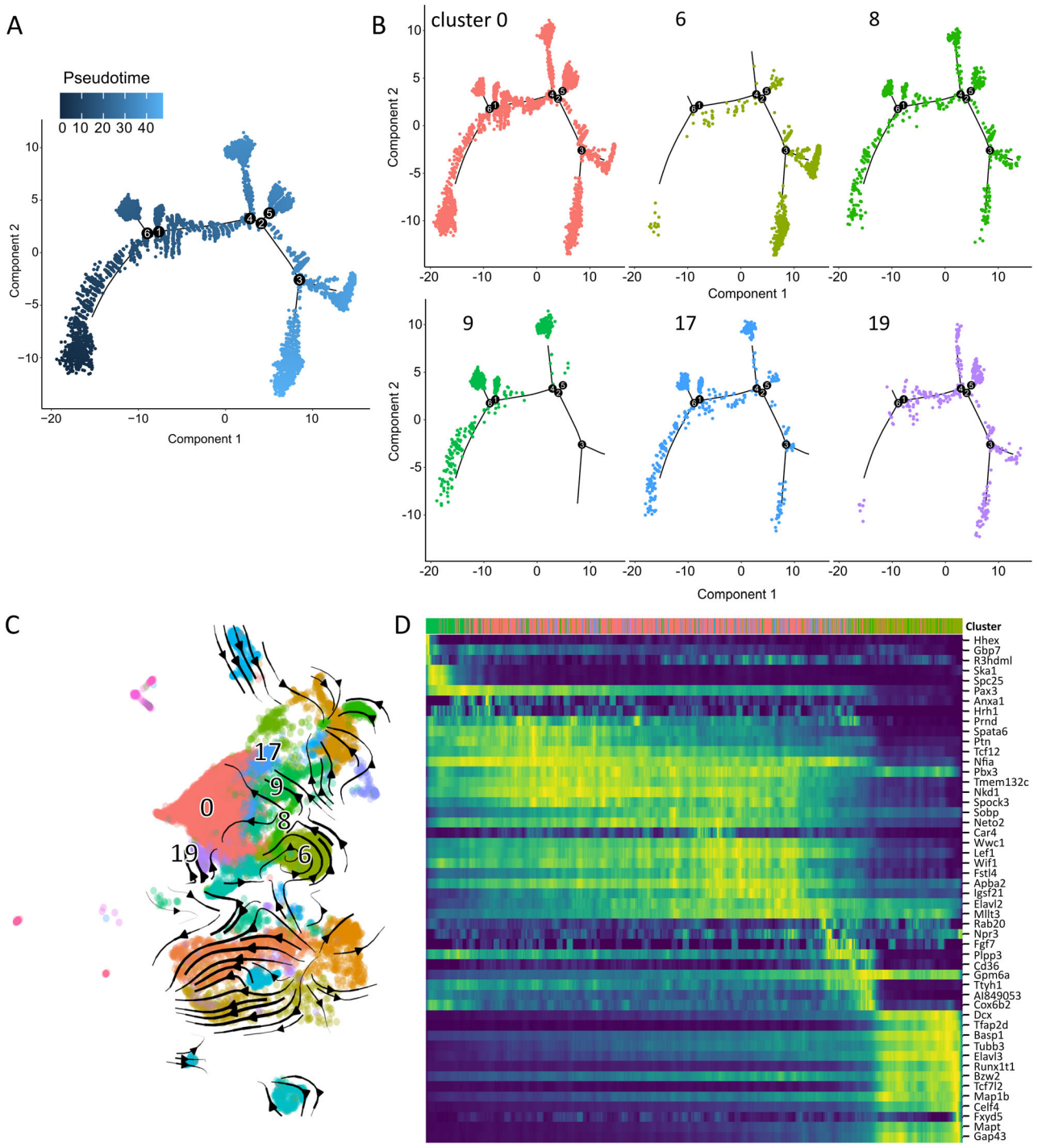

Figure 12. Single-cell trajectory and RNA velocity analysis of mutant cerebellum. ***A***, ***B***, Trajectory analysis of single cells from mutant (*Blbp-cre::Ctnnb1(ex3)$^{fl/wt}$::Smarca4$^{fl/rec}$*) E16.5 cerebella with (***A***) pseudotime of all cells shown or (***B***) cells of each cluster (according to UMAP in Fig. 11) depicted separately. Cells of Cluster 9 are rather situated at the beginning of the trajectory, Cluster 0 is distributed along the whole trajectory, and Cluster 6 forms the main cell population at the end of the trajectory. ***C***, RNA velocity analysis according to RNA splicing applied as stream onto UMAP embedding of mutant cells (as shown in Fig. 11). Cells are transitioning from Cluster 9 to Cluster 0, within which there is less dynamic change. ***D***, Cells are ordered according to their latent time in RNA velocity analysis, showing a transition from Cluster 9 to Cluster 6 via Cluster 0. Standardized expression of genes selected by fit-likelihood to the model is shown in the heatmap.

HPCs migrating from the explants. Consequently, the scaffold provided by the extracellular matrix and a variety of surrounding embryonic cell types might play an important role in the development of lesions. Therefore, transplantation of mutant HPCs into younger mice such as P0 pups might provide a more suitable environment for the development of tumors (Ho et al., 2020; Olivetti et al., 2020).

Altogether, our new mouse model provides the first evidence for a cooperative effect of aberrant WNT signaling and a SMARCA4 deficiency in driving cell transformation. Our findings on deregulated genes and pathways involved and the suggested importance of the tumor microenvironment might pave the way to identify new therapeutic targets for tumors affected by both alterations.

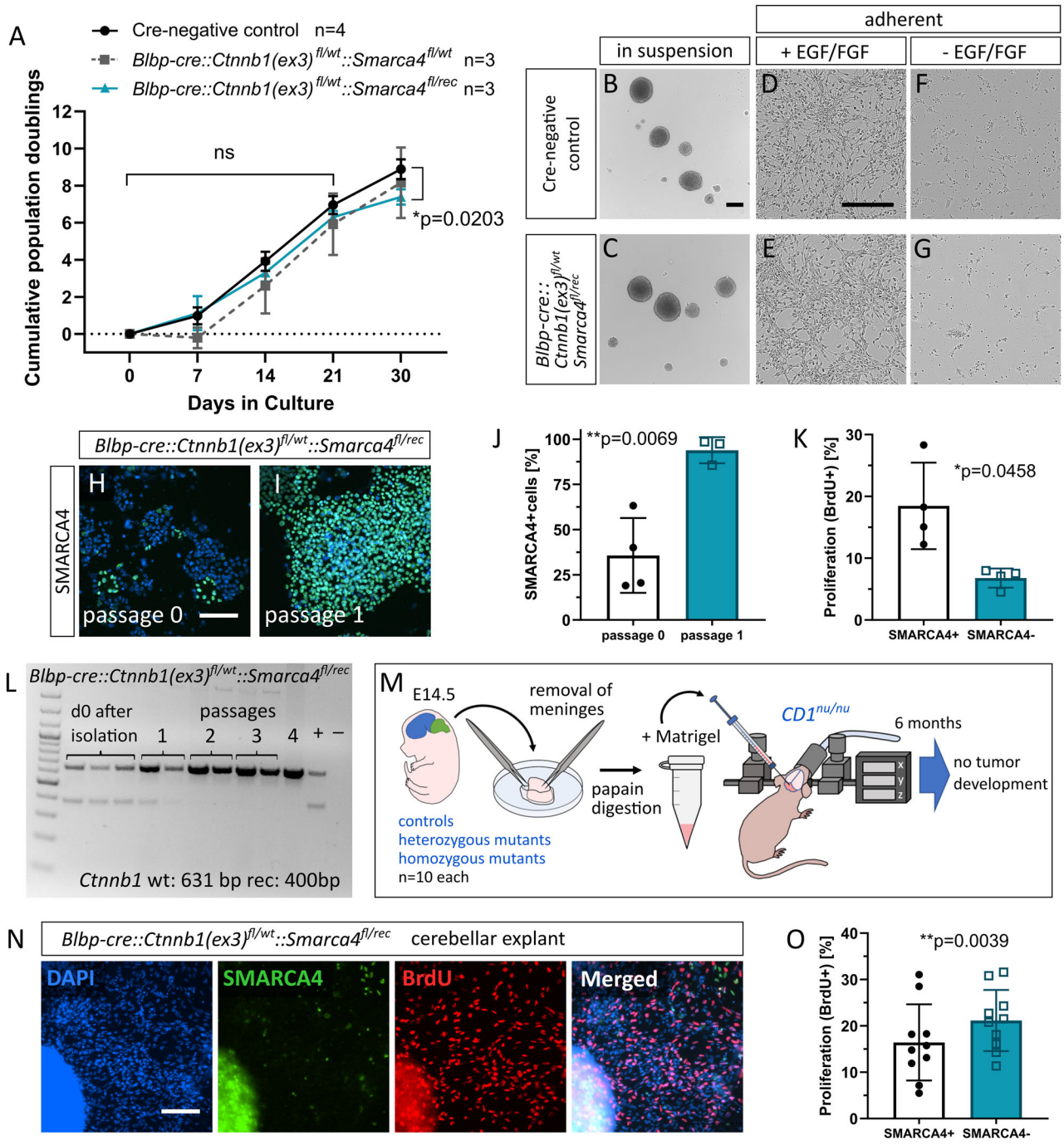

Figure 13. Mutant cerebellar cells show decreased growth in vitro and no tumorigenic potential after transplantation but increased proliferation when cultured as cerebellar explants. ***A***, Cumulative PD of HPCs grown as neurospheres isolated at E14.5 from controls, heterozygous mutants (*Blbp-cre::Ctnnb1(ex3)*$^{fl/wt}$*::Smarca4*$^{fl/wt}$), and homozygous mutants (*Blbp-cre::Ctnnb1(ex3)*$^{fl/wt}$*::Smarca4*$^{fl/rec}$) with weekly passaging. No significant difference observed on Days 7, 14, and 21 in culture but slightly reduced cumulative PD in homozygous mutants vs controls at Day 30 (mean = 7.390 and 8.884, respectively; Tukey's multiple-comparisons test after two-way ANOVA, adjusted $p = 0.023$, $q = 5.884$, DF = 4.964). *N* corresponds to biological replicates . ***B***, ***C***, Morphologically, neurospheres of controls and homozygous mutants do not differ from each other (both Passage 0). ***D***–***G***, Both mutant and control HPCs show adherent growth when seeded in PLO-coated wells after dissociation with a dependency on EGF/FGF for cell growth (both Passage 1, 4 d after seeding). ***H***–***J***, SMARCA4 IF staining of neurosphere cytospins shows a loss of SMARCA4 at Passage 0 (Day 7) in the majority of cells, which is almost undetectable at Passage 1 (Day 14). ***J***, Statistic evaluation of SMARCA4 IF stainings shows an increase of SMARCA4-positive cells in mutant HPC neurosphere cultures from Passage 0 to Passage 1. ***K***, IF costaining of SMARCA4 and BrdU in mutant HPC neurospheres at Passage 0 reveals significantly reduced proliferation of SMARCA4-deficient cells. ***L***, PCR for recombined *Ctnnb1* with DNA isolated from mutant HPC neurosphere pellets at isolation and at Passages 1–4. ***M***, Transplantation of E14.5 hindbrains ($n = 10$ of each control, heterozygous mutants, and homozygous mutants) into immunodeficient *CD1*$^{nu/nu}$ mice did not result in tumor development. ***N***, SMARCA4 and BrdU IF costaining of *Blbp-cre::Ctnnb1(ex3)*$^{fl/wt}$*::Smarca4*$^{fl/rec}$ E14.5 cerebellar explants at Day 4 of culture. ***O***, SMARCA4-negative cells show significantly higher proliferation compared with SMARCA4-positive cells in *Blbp-cre::Ctnnb1(ex3)*$^{fl/wt}$*::Smarca4*$^{fl/rec}$ cerebellar explant culture as evaluated by IF stainings ($t = 3.697$, DF = 9, $p = 0.0049$, paired *t* test). Scale bar in ***B*** corresponds to 200 µm (applicable to ***C***), in ***D*** to 200 µm (applicable to ***E***–***G***), and in ***H*** and ***N*** to 100 µm (applicable to ***I***).

Data Availability

Raw and processed data may be obtained from Gene Expression Omnibus under the accession numbers GSE240627 for DNA methylation data and GSE241018 for single-cell RNA sequencing data. All other data or materials used in this study are available upon request.

References

Ahlers KE, Chakravarti B, Fisher RA (2016) RGS6 as a novel therapeutic target in CNS diseases and cancer. AAPS J 18:560–572.

Alfert A, Moreno N, Kerl K (2019) The BAF complex in development and disease. Epigenetics Chromatin 12:19.

Aryee MJ, Jaffe AE, Corrada-Bravo H, Ladd-Acosta C, Feinberg AP, Hansen KD, Irizarry RA (2014) Minfi: a flexible and comprehensive Bioconductor package for the analysis of Infinium DNA methylation microarrays. Bioinformatics 30:1363–1369.

Benavides F, Rülicke T, Prins JB, Bussell J, Scavizzi F, Cinelli P, Herault Y, Wedekind D (2020) Genetic quality assurance and genetic monitoring of laboratory mice and rats: FELASA Working Group Report. Lab Anim 54:135–148.

Bögershausen N, Wollnik B (2018) Mutational landscapes and phenotypic spectrum of SWI/SNF-related intellectual disability disorders. Front Mol Neurosci 11:252.

Capper D, et al. (2018) DNA methylation-based classification of central nervous system tumours. Nature 555:469–474.

Clapier CR, Iwasa J, Cairns BR, Peterson CL (2017) Mechanisms of action and regulation of ATP-dependent chromatin-remodelling complexes. Nat Rev Mol Cell Biol 18:407–422.

Dermietzel R, Krause D, Kremer M, Wang C, Stevenson B (1992) Pattern of glucose transporter (Glut 1) expression in embryonic brains is related to maturation of bood-brain barrier tightness. Dev Dyn 193:152–163.

Engelkamp D, Rashbass P, Seawright A, van Heyningen V (1999) Role of Pax6 in development of the cerebellar system. Development 126:3585–3596.

Fernando TM, et al. (2020) Functional characterization of SMARCA4 variants identified by targeted exome-sequencing of 131,668 cancer patients. Nat Commun 11:5551.

Gajjar A, et al. (2021) Outcomes by clinical and molecular features in children with medulloblastoma treated with risk-adapted therapy: results of an international phase III trial (SJMB03). J Clin Oncol 39:822–835.

Gajjar A, Finlay JL (2015) The management of children and adolescents with medulloblastoma in low and middle income countries. Pediatr Blood Cancer 62:549–550.

Gatto L, Franceschi E, Tosoni A, Di Nunno V, Bartolini S, Brandes AA (2022) Molecular targeted therapies: time for a paradigm shift in medulloblastoma treatment? Cancers (Basel) 14:333.

Gibson P, et al. (2010) Subtypes of medulloblastoma have distinct developmental origins. Nature 468:1095–1099.

Goschzik T, et al. (2022) Genetic alterations of TP53 and OTX2 indicate increased risk of relapse in WNT medulloblastomas. Acta Neuropathol 144:1143–1156.

Gu Z, Eils R, Schlesner M (2016) Complex heatmaps reveal patterns and correlations in multidimensional genomic data. Bioinformatics 32:2847–2849.

Hall A (2009) The cytoskeleton and cancer. Cancer Metastasis Rev 28:5–14.

Hao Y, et al. (2021) Integrated analysis of multimodal single-cell data. Cell 184:3573–3587.

Harada N, Tamai Y, Ishikawa T, Sauer B, Takaku K, Oshima M, Taketo MM (1999) Intestinal polyposis in mice with a dominant stable mutation of the beta-catenin gene. EMBO J 18:5931–5942.

Hasselblatt M, et al. (2014) SMARCA4-mutated atypical teratoid/rhabdoid tumors are associated with inherited germline alterations and poor prognosis. Acta Neuropathol 128:453–456.

Hayashi S, Tenzen T, McMahon AP (2003) Maternal inheritance of Cre activity in a Sox2Cre deleter strain. Genesis 37:51–53.

Hegedus B, Dasgupta B, Shin JE, Emnett RJ, Hart-Mahon EK, Elghazi L, Bernal-Mizrachi E, Gutmann DH (2007) Neurofibromatosis-1 regulates neuronal and glial cell differentiation from neuroglial progenitors in vivo by both cAMP- and Ras-dependent mechanisms. Cell Stem Cell 1: 443–457.

Ho H, Fowle A, Coetzee M, Greger IH, Watson JF (2020) An inhalation anaesthesia approach for neonatal mice allowing streamlined stereotactic injection in the brain. J Neurosci Methods 342:e108824.

Hodges HC, Stanton BZ, Cermakova K, Chang CY, Miller EL, Kirkland JG, Ku WL, Veverka V, Zhao K, Crabtree GR (2018) Dominant-negative SMARCA4 mutants alter the accessibility landscape of tissue-unrestricted enhancers. Nat Struct Mol Biol 25:61–72.

Holdhof D, et al. (2021a) Brahma-related gene 1 has time-specific roles during brain and eye development. Development 148:e196147.

Holdhof D, et al. (2021b) Atypical teratoid/rhabdoid tumors (ATRTs) with SMARCA4 mutation are molecularly distinct from SMARCB1-deficient cases. Acta Neuropathol 141:291–301.

Holdhof D, Schoof M, Hellwig M, Holdhof NH, Niesen J, Schuller U (2020) hGFAP-positive stem cells depend on Brg1 for proper formation of cerebral and cerebellar structures. Cereb Cortex 30:1382–1392.

Indra AK, Dupé VR, Bornert J-M, Messaddeq N, Yaniv M, Mark M, Chambon P, Metzger D (2005) Temporally controlled targeted somatic mutagenesis in embryonic surface ectoderm and fetal epidermal keratinocytes unveils two distinct developmental functions of BRG1 in limb morphogenesis and skin barrier formation. Development 132:4533–4544.

Jessa S, et al. (2019) Stalled developmental programs at the root of pediatric brain tumors. Nat Genet 51:1702–1713.

Jin Y, et al. (2021) Long noncoding RNA PM maintains cerebellar synaptic integrity and Cbln1 activation via Pax6/Mll1-mediated H3K4me3. PLoS Biol 19:e3001297.

Jo JH, Park SB, Park S, Lee HS, Kim C, Jung DE, Song SY (2019) Novel gastric cancer stem cell-related marker LINGO2 Is associated with cancer cell phenotype and patient outcome. Int J Mol Sci 20:555.

Kim S, Jeong S (2019) Mutation hotspots in the β-catenin gene: lessons from the human cancer genome databases. Mol Cells 42:8–16.

La Manno G, et al. (2021) Molecular architecture of the developing mouse brain. Nature 596:92–96.

Latour M, Her NG, Kesari S, Nurmemmedov E (2021) WNT signaling as a therapeutic target for glioblastoma. Int J Mol Sci 22:e8428.

Liu J, Willet SG, Bankaitis ED, Xu Y, Wright CV, Gu G (2013) Non-parallel recombination limits Cre-LoxP-based reporters as precise indicators of conditional genetic manipulation. Genesis 51:436–442.

Liu J, Xiao Q, Xiao J, Niu C, Li Y, Zhang X, Zhou Z, Shu G, Yin G (2022) Wnt/β-catenin signalling: function, biological mechanisms, and therapeutic opportunities. Signal Transduct Target Ther 7:3.

Luo L, et al. (2020) Optimizing nervous system-specific gene targeting with Cre driver lines: prevalence of germline recombination and influencing factors. Neuron 106:37–65.

Luo Z, et al. (2021) Genomic and transcriptomic analyses reveals ZNF124 as a critical regulator in highly aggressive medulloblastomas. Front Cell Dev Biol 9:634056.

Martinez S, Andreu A, Mecklenburg N, Echevarria D (2013) Cellular and molecular basis of cerebellar development. Front Neuroanat 7:18.

Matsumoto S, Banine F, Struve J, Xing R, Adams C, Liu Y, Metzger D, Chambon P, Rao MS, Sherman LS (2006) Brg1 is required for murine neural stem cell maintenance and gliogenesis. Dev Biol 289:372–383.

McInnes L, Healy J, Saul N, Großberger L (2018) UMAP: uniform manifold approximation and projection. J Open Source Softw 3:e861.

Meixner A, Haverkamp S, Wässle H, Führer S, Thalhammer J, Kropf N, Bittner RE, Lassmann H, Wiche G, Propst F (2000) MAP1B is required for axon guidance and Is involved in the development of the central and peripheral nervous system. J Cell Biol 151:1169–1178.

Mosimann C, Hausmann G, Basler K (2009) β-Catenin hits chromatin: regulation of Wnt target gene activation. Nat Rev Mol Cell Biol 10: 276–286.

Mynarek M, Milde T, Padovani L, Janssens GO, Kwiecien R, Mosseri V, Clifford SC, Doz F, Rutkowski S (2021) SIOP PNET5 MB trial: history and concept of a molecularly stratified clinical trial of risk-adapted therapies for standard-risk medulloblastoma. Cancers (Basel) 13:e6077.

Northcott PA, et al. (2017) The whole-genome landscape of medulloblastoma subtypes. Nature 547:311–317.

Nürnberg A, Kitzing T, Grosse R (2011) Nucleating actin for invasion. Nat Rev Cancer 11:177–187.

Olivetti PR, Lacefield CO, Kellendonk C (2020) A device for stereotaxic viral delivery into the brains of neonatal mice. Biotechniques 69:307–312.

Orr BA (2020) Pathology, diagnostics, and classification of medulloblastoma. Brain Pathol 30:664–678.

Pan N, Jahan I, Lee JE, Fritzsch B (2009) Defects in the cerebella of conditional Neurod1 null mice correlate with effective Tg(Atoh1-cre) recombination and granule cell requirements for Neurod1 for differentiation. Cell Tissue Res 337:407–428.

Pardridge WM, Boado RJ, Farrell CR (1990) Brain-type glucose transporter (GLUT-1) is selectively localized to the blood-brain barrier. Studies with quantitative western blotting and in situ hybridization. J Biol Chem 265:18035–18040.

Phoenix TN, et al. (2016) Medulloblastoma genotype dictates blood brain barrier phenotype. Cancer Cell 29:508–522.

Pöschl J, Grammel D, Dorostkar MM, Kretzschmar HA, Schüller U (2013) Constitutive activation of β-catenin in neural progenitors results in disrupted proliferation and migration of neurons within the central nervous system. Dev Biol 374:319–332.

Ramos P, et al. (2014) Loss of the tumor suppressor SMARCA4 in small cell carcinoma of the ovary, hypercalcemic type (SCCOHT). Rare Dis 2: e967148.

Ren X, Kuan PF (2019) methylGSA: a Bioconductor package and Shiny app for DNA methylation data length bias adjustment in gene set testing. Bioinformatics 35:1958–1959.

Requardt RP, Kaczmarczyk L, Dublin P, Wallraff-Beck A, Mikeska T, Degen J, Waha A, Steinhäuser C, Willecke K, Theis M (2009) Quality control of astrocyte-directed Cre transgenic mice: the benefits of a direct link between loss of gene expression and reporter activation. Glia 57:680–692.

Robinson G, et al. (2012) Novel mutations target distinct subgroups of medulloblastoma. Nature 488:43–48.

Sanchez-Pulido L, Ponting CP (2018) TMEM132: an ancient architecture of cohesin and immunoglobulin domains define a new family of neural adhesion molecules. Bioinformatics 34:721–724.

Seto Y, et al. (2014) Temporal identity transition from Purkinje cell progenitors to GABAergic interneuron progenitors in the cerebellum. Nat Commun 5:3337.

Shannon P, Markiel A, Ozier O, Baliga NS, Wang JT, Ramage D, Amin N, Schwikowski B, Ideker T (2003) Cytoscape: a software environment for integrated models of biomolecular interaction networks. Genome Res 13:2498–2504.

Sharma T, et al. (2019) Second-generation molecular subgrouping of medulloblastoma: an international meta-analysis of Group 3 and Group 4 subtypes. Acta Neuropathol 138:309–326.

Sharma T, Olea-Flores M, Imbalzano AN (2023) Regulation of the Wnt signaling pathway during myogenesis by the mammalian SWI/SNF ATPase BRG1. Front Cell Dev Biol 11:1160227.

Stevens JC, Banks GT, Festing MF, Fisher EM (2007) Quiet mutations in inbred strains of mice. Trends Mol Med 13:512–519.

Stuart T, Butler A, Hoffman P, Hafemeister C, Papalexi E, Mauck WM 3rd, Hao Y, Stoeckius M, Smibert P, Satija R (2019) Comprehensive integration of single-cell data. Cell 177:1888–1902.e1821.

Sumi-Ichinose C, Ichinose H, Metzger D, Chambon P (1997) SNF2beta-BRG1 is essential for the viability of F9 murine embryonal carcinoma cells. Mol Cell Biol 17:5976–5986.

Supek F, Bošnjak M, Škunca N, Šmuc T (2011) REVIGO summarizes and visualizes long lists of gene ontology terms. PLoS ONE 6:e21800.

Taylor MD, et al. (2012) Molecular subgroups of medulloblastoma: the current consensus. Acta Neuropathol 123:465–472.

Thompson EM, Ashley D, Landi D (2020) Current medulloblastoma subgroup specific clinical trials. Transl Pediatr 9:157–162.

Tischfield MA, et al. (2010) Human TUBB3 mutations perturb microtubule dynamics, kinesin interactions, and axon guidance. Cell 140:74–87.

van Essen MJ, Nayler S, Becker EBE, Jacob J (2020) Deconstructing cerebellar development cell by cell. PLoS Genet 16:e1008630.

Vogel P, Read RW, Hansen GM, Payne BJ, Small D, Sands AT, Zambrowicz BP (2012) Congenital hydrocephalus in genetically engineered mice. Vet Pathol 49:166–181.

Vuong CK, et al. (2018) Rbfox1 regulates synaptic transmission through the inhibitory neuron-specific vSNARE Vamp1. Neuron 98:127–141.e127.

Wieczorek D, et al. (2013) A comprehensive molecular study on Coffin-Siris and Nicolaides-Baraitser syndromes identifies a broad molecular and clinical spectrum converging on altered chromatin remodeling. Hum Mol Genet 22:5121–5135.

Wilson PG, Stice SS (2006) Development and differentiation of neural rosettes derived from human embryonic stem cells. Stem Cell Rev 2:67–77.

Zhang N, et al. (2011) Foxm1 promotes β-catenin nuclear localization and controls Wnt target-gene expression and glioma tumorigenesis. Cancer Cell 20:427–442.

Zhang T, et al. (2021) Generation of excitatory and inhibitory neurons from common progenitors via Notch signaling in the cerebellum. Cell Rep 35: e109208.

Zhang X, Lin P-Y, Liakath-Ali K, Südhof TC (2022) Teneurins assemble into presynaptic nanoclusters that promote synapse formation via postsynaptic non-teneurin ligands. Nat Commun 13:2297.

Zheng GXY, et al. (2017) Massively parallel digital transcriptional profiling of single cells. Nat Commun 8:14049.

Zhou W, Triche TJ Jr, Laird PW, Shen H (2018) SeSAMe: reducing artifactual detection of DNA methylation by Infinium BeadChips in genomic deletions. Nucleic Acids Res 46:e123–e123.